Title	Coseismic dehydration of serpentinite: Evidence from high-velocity friction experiments
Author(s)	Lin, Aiming; Takano, Soichiro; Hirono, Tetsuro; Kanagawa, Kyuichi
Citation	Chemical Geology (2013), 344: 50-62
Issue Date	2013-04-19
URL	http://hdl.handle.net/2433/179481
Right	© 2012 Published by Elsevier B.V.
Type	Journal Article
Textversion	author

Coseismic dehydration of serpentinite: Evidence from high-velocity friction experiments

Aiming Lin[1]*, Soichiro Takano[2], Tetsuro Hirono[3], Kyuichi Kanagawa[4]

[1]Department of Geophysics, Graduate School of Science, Kyoto University, Kyoto 606-8502, Japan

[2]Institute of Geosciences, Faculty of Science, Shizuoka University Shizuoka 422-8529, Japan

[3]Department of Earth and Space Science, Graduate School of Science, Osaka University, Toyonaka 500-0043, Japan

[4]Department of Earth Sciences, Chiba University, Chiba, Japan

*Corresponding author:
Department of Geophysics
Graduate School of Science
Kyoto University
Kyoto 606-8502, Japan
Tel & Fax: 81-76-753-394
E-mail: slin@kugi.kyoto-u.ac.jp

ABSTRACT

High-velocity friction (HVF) experiments on serpentinite under conditions equivalent to large amounts of earthquake slip produced large volumes of water vapor derived from the frictional-heating-induced dehydration of serpentinite. Fourier Transform Infrared (FTIR) and thermogravimetry (TG)-Differential Scanning Calorimetry (DSC) microspectroscopic analyses show that the water in the slip zone and its bounding zones was released due to dehydration during the HVF experiments. Our experimental results demonstrate that (i) the run product consists of ~10 wt.% molten materials with abundant vesicles and ~90 wt.% fine-grained clasts; (ii) both serpentine and olivine minerals were melted during high-velocity slip (1.1–1.3 m/s); (iii) rapid serpentine dehydration occurred in a zone of up to ~3 mm wide, including the slip zone and its bounding zones, accompanying frictional melting during high-velocity slip; and (iv) no distinct dehydration or frictional melting occurred during low-velocity slip (<0.4 m/s). These findings show that dehydration reactions of serpentine can be caused by frictional heating that accompanies frictional melting in the slip zone, and by the rapid diffusion of frictional heat from the main slip zone to a wide zone bounded by the coseismic slip plane during seismic faulting. The present results reveal that the thermal pressurization caused by the dehydration of serpentine and frictional melting is a main mechanism that may lead to the dynamic weakening of seismogenic faults, thereby facilitating seismic slip during large earthquakes in subduction zones and along intracontinental faults that contain abundant hydrous minerals.

Keywords: dehydration, serpentinite, high-velocity slip, fault strength, dynamic

48 weakening of seismogenic fault, thermal pressurization

49

50 **1. Introduction**

51

52 Thermal pressurization has been proposed as a major mechanism of lowering the
53 dynamic strength of faults during earthquake slip [e.g., Sibson, 1973; Lachenbruch,
54 1980; Andrews, 2002; Wibberley and Shimamoto, 2005]. A commonly invoked
55 mechanism of thermal pressurization in this regard is a reduction in effective normal
56 stress induced by the sudden increase in pore pressure that arises from the release of
57 fluid via dehydration reactions [e.g., Meade and Jeanloz, 1991; Tibi et al., 2002]. In
58 recent years, many experimental studies have suggested that thermal pressurization may
59 result from mineral decomposition, such as the dehydration of serpentine or kaolinite
60 [e.g., Hirose and Bystricky, 2007; Brantut et al., 2008; Viti and Hirose, 2010; Kohli et
61 al., 2011], the decarbonation of calcite or siderite [Han et al., 2007, 2010], and the
62 dehydration of gypsum [Brantut et al., 2011]. Observations of natural seismogenic fault
63 cores that contain fault gouges also support the supposition that dehydration reactions
64 occur during seismic faulting [e.g., Famin et al., 2008; Hamada et al., 2009, 2011].
65 Serpentine is closely associated with transform faults [e.g., Christensen, 1972;
66 Francis, 1981; Moore and Rymer, 2007] and with seismogenic faults within subduction
67 zones [Ulmer and Trommsdorff, 1995]; indeed, the presence of serpentine minerals is
68 considered to facilitate creep along the San Andreas Fault [Moore and Rymer, 2007],
69 thereby explaining its low fault strength [Wibberley, 2007]. In numerical modeling, heat
70 diffusion is considered an important coupling factor of thermal pressurization, which

71 occurs normal to the slip zone [Brantut et al., 2010]. Should serpentine dehydration
72 occur due to frictional heating along seismogenic faults and should heat diffusion occur
73 within a wide dehydration reaction zone bounded by the slip zone during earthquake slip,
74 it is likely that a considerable volume of water would be released from serpentine-rich
75 slip zones and their bounding zones. Thus, it is proposed that a rapid dehydration
76 reaction involving serpentine would induce a sudden increase in fluid pressure that
77 would simultaneously act to reduce the effective normal stress and markedly weaken the
78 dynamic strength of seismogenic faults during seismic faulting.
79 To test this hypothesis, a low- to high-velocity rotary shear test apparatus [Lin, 2008]
80 was used to conduct uniaxial high-velocity friction (HVF) experiments under conditions
81 equivalent to large earthquake slip with various slip rates, using natural serpentinite
82 samples from Nagano Prefecture, Japan. This paper describes the results of these
83 experiments, which showed the instantaneous dehydration of serpentinite due to
84 frictional heating along the simulated fault and heat diffusion within a wide zone
85 bounded by the slip zone.
86
87 **2. Experimental Procedure and Conditions**
88
89 ***2.1. Test Equipment***
90
91 All of the present experiments on frictional-heating-induced hydration of serpentine
92 were performed under dry conditions using a rotary-shear low- to high-velocity
93 frictional test machine installed at Shizuoka University, Japan (Fig. 1). This machine

94 contains two testing devices: a uniaxial rotary-shear low- to high-velocity friction device
95 that lacks a hydraulic pressure vessel [as used by Lin and Shimamoto, 1998], and a
96 hydraulic friction apparatus with a controlling device for high pore-water pressure,
97 attached to the uniaxial rotary-shear low- to high-velocity friction device (Figs 1 and 2).
98 This device has a wide range of slip rates, from <10 cm/yr to 10 m/s, yielding
99 mechanical data such as torque, the frictional coefficient, amount of axial shortening,
100 normal stress and shear stress, pore-water pressure, frictional melt temperature, and
101 displacement. The test equipment can be used to apply normal stresses up to
102 approximately 100 MPa, close to the typical uniaxial strength of crystalline rocks,
103 provided that anvil-shaped specimens are used. In practical use, however, it is only
104 possible to apply normal stresses of <15 MPa because of the severe thermal fracturing
105 of unconfined specimens that occurs upon frictional heating.
106
107 ***2.2. Experimental Conditions***
108
109 Serpentinite samples for the experiments, collected from Nagano Prefecture, central
110 Japan, were free of visible cracks and consisted of ~65% antigorite and ~35% olivine,
111 along with trace amounts of mafic minerals (Fig. 3).
112 Ten HVF experiments were performed at room temperature under dry conditions and
113 with equivalent slip rates [Shimamoto and Tsutsumi, 1994; Lin and Shimamoto, 1998]
114 of 1.10–1.31 m/s and normal stresses of 2–9 MPa (Table 1). In such experiments, the
115 slip rate varies from the inner to outer circumferences of the sample, so we used the
116 equivalent slip rate (Veq), which is defined as Veq multiplied by the area of sliding

117 equals the rate of frictional work. Assuming a constant frictional coefficient over the
118 sliding surface, Veq for a cylindrical specimen of diameter r is given by

119 $$Veq = 4/3\ \pi\ r\ R$$

120 where R is the revolution rate of the motor [Shimamoto and Tsutsumi, 1994].
121 Low-velocity (0.35–0.4 m/s) friction (LVF) experiments were conducted for comparison
122 with the results of the HVF experiments (Table 2). A pair of cylindrical specimens (25
123 mm in diameter and 50 mm in length) was used in each experiment, with the circular
124 interface between the two specimens being set as the slip plane (Fig. 2). The sliding
125 surfaces were polished with 1500# SiC powders. Because large normal stresses could
126 not be applied to the simulated fault due to the limitations of the experimental apparatus,
127 the HVF experiments were run over a period of ~15–40 sec, corresponding to
128 displacements of 20–50 m. These displacements are comparable with those recorded
129 during large-magnitude earthquakes (e.g., maximum displacements of 15–30 m have
130 been reported for the 2001 M_w 7.8 Kunlun earthquake [Lin et al., 2002], the 2004 M_w
131 9.0 Sumatra–Andaman earthquake [Subarya et al., 2006], and the 2011 M_w 9.0 Offshore
132 Tohoku (Japan) earthquake [Yagi and Fukahata, 2011]). In contrast, the total
133 displacements over a period of ~15–40 sec in the LVF experiments were calculated to
134 be 5–15 m. The frictional energy expended per unit area in the experiments under a slip
135 rate of ~1 m/s and a large displacement of up to 50 m is similar to that expended during
136 a medium- to large-magnitude crustal earthquake [O'Hara et al., 2006], at least in terms
137 of slip velocity and stress drop [Kanamori and Brodsky, 2004].
138 Serpentine dehydration phenomena were directly observed during the HVF
139 experiments (1.10–1.31 m/s) through a transparent window cover on the experimental

apparatus (Fig. 4). The simulated fault began to produce water vapor and dust within 0.2 sec of the initiation of fault motion (Fig. 4a). Water vapor, accompanied by sparks and red melt material, was sprayed out from the slip zone, with some instantaneously cooling to water droplets (0.1–5.0 mm in diameter) on the transparent window cover (Fig. 4b–d). The ejection of water vapor from the simulated fault continued until the end of each experiment, with the droplets on the window cover forming a band of 3–7 mm in width (Fig. 4b–d). In contrast, such water vapor and water droplets were not observed during the LVF experiments.

3. Results

3.1. Microstructures of Run Products

The slip zones that formed during the experiments ranged in width from 0.1 to 2.0 mm, consisting of numerous fractured fragments of olivine within a very fine-grained matrix that was too fine to enable the identification of minerals (Figs 5 and 6), even by powder X-ray diffraction analysis. The olivine crystals abutting the slip zone were generally fractured, with numerous cracks infilled by molten run products containing fine-grained clasts, forming complex network veins branching from the main slip zone (Fig. 5a). These veins resemble natural pseudotachylyte veins in their geometry and morphology [Lin, 2008]. In contrast, the antigorite crystals that abut the slip zone were mainly decomposed, without distinct cracks or fibrous textures as those observed in the host rock far from the slip zone (Figs 5 and 6a–c). These textural features indicate that

163 the serpentine crystals were decomposed in a narrow zone of <3 mm width, developed
164 each side of the slip zone, within which the serpentine was subjected to dehydration
165 reactions during the HVF experiments (see below for details).
166 Some molten run products were extruded from the simulated fault after 0.5 sec of the
167 onset of slip, occurring as irregular branch-like forms of <2 mm in diameter and up to 3
168 cm in length, showing flow structure and with a vitreous luster similar to that of fresh
169 lava (Fig. 7a). Molten material that includes numerous fine-grained clasts is generally
170 heterogeneous in texture under the microscope, showing flow structure and containing
171 numerous spherical to elliptical vesicles ranging in diameter from sub-micron size to 0.5
172 mm (Figs 6d and 7b). Such vesicular structures are considered to form via the extrusion
173 of gas (water vapor) from a melt during frictional melting, as reported previously in both
174 natural pseudotachylyte [e.g., Maddock et al., 1987; Lin, 1994, 2008; Magloughlin,
175 2011] and experimentally generated pseudotachylyte [Lin and Shimamoto, 1998]. These
176 structural features observed in the present experiments indicate that molten material
177 formed and water vapor was released from the slip zone during the HVF experiments
178 (Fig. 4).
179 The vesicles and flow structures are observed in narrow zones of <3 mm wide
180 bounded by antigorite crystals on each side of the slip zone (Figs 5a and 6a–c). The
181 fibrous textures of antigorite crystals observed in the starting serpentine samples are not
182 recognized in the dehydration zones that abut the slip zone (Figs 5b and 6a–c).
183
184 ***3.2. Powder X-ray Diffraction Analysis***
185

186 Two types of run products were analyzed by powder X-ray diffraction method: one is
187 the molten material remained in the slip zone (HVF R001), and another is the molten
188 material of run product extruded from the slip zone during the HVF experiment (HVF
189 R012). For comparison with the run products, the host serpentinite sample and olivine
190 mineral sample were also analyzed. Powder X-ray diffraction analyses reveal that the
191 diffraction peaks of antigorite are absent from the spectra of the run products, even
192 though antigorite made up ~65% of the starting samples (Fig. 8). The integrated
193 intensities of olivine peaks in the spectra for run materials (Fig. 8c, d) are slightly
194 stronger than those for the serpentinite sample (Fig. 8a). The diffraction spectra of both
195 types of run products contain a distinctive, broad band ranging from 2θ values of 12° to
196 42°, comparable with that for a standard sample containing 5–10 wt.% glass (Fig. 8d–f).
197 These diffraction patterns are also comparable with the XRD spectra of standard
198 samples analyzed for the quantitative calibration of glassy materials contained in the
199 HVF experimentally generated pseudotachylyte, as reported by Lin and Shimamoto
200 (1998). This finding indicates that up to 10 wt.% glass or amorphous material formed in
201 the run products that were extruded and remained in the slip zone during the present
202 experiments, as observed under optical and electron microscopes (Figs 5 and 6).
203
204 ***3.3. Chemical Compositions***
205
206 The bulk chemical composition of serpentinite samples used in the frictional
207 experiments was analyzed by X-ray fluorescence (XRF) (sample Host1 in Table 2). For
208 comparison with the run products, the chemical composition of serpentine and olivine

minerals in samples of host rock (samples HS1-HS5 and HO1-2 in Table 2) was measured using an electron-probe microanalyzer (EPMA, JXA733). The chemical compositions of run products in the slip zone and in the dehydration zones (Fig. 5) were measured from a thin section oriented perpendicular to the slip zone, as shown in Fig. 3c (Tables 3–4).

The molten materials derived from the slip zone are generally heterogeneous in chemical composition (Fig. 9, Table 3), which differs from the bulk composition of the host rock, and from that of serpentine and olivine minerals contained in the host rock, respectively (Fig. 9, Table 2). The serpentine minerals in the dehydration zones (samples Dh1–Dh8 in Table 4) have a similar composition with that of serpentine minerals in the host rock with the sum of elements of 2.82-2.84 (Fig. 9, samples HS1–HS6, in Table 2). The variation diagrams of major oxides show a characteristic change in SiO_2, MgO, FeO, CaO and Al_2O_3 components in the run products (Fig. 9). Comparing with the dehydration zones, the molten materials in the slip zone have lower SiO_2 and Al_2O_3 components and higher FeO component similar to that of olivine minerals contained in the host rock (Fig. 9). The slip zone has a large variation range in CaO and FeO components which are generally higher than that of serpentine minerals contained in the host serpentinite. There is also a large variation range in MgO component of the molten materials. In contrast, there is a small variation range in MgO component in serpentine minerals contained in the host serpentinite and dehydration zone (Fig. 9). The variations of chemical composition in the molten materials may be caused by friction melting of serpentine and olivine minerals, in which molten materials were not completely mixed and contaminated.

232 The analytical totals of the molten materials in the slip zone and serpentine minerals
233 that abut the slip zone are up to >97.6–99.6 wt.% (Tables 3–4), higher than that of
234 serpentine minerals in the host rock (samples HS1–HS6 in Table 2). These high total
235 amounts can be interpreted as a result of water release from the slip zone and bounding
236 zones due to the dehydration of serpentine minerals (see below for details).
237
238 ***3.4. Frictional Coefficient and Shortening Amount***
239
240 The frictional coefficient μ showed an immediate increase to 0.56 at the onset of slip,
241 within the first 0.1 sec of the experiments, but just as quickly dropped to a steady-state
242 value of 0.23 prior to an elapsed time of 0.2 sec during the HVF experiments (Fig.
243 10a–b). This pronounced peak in friction accompanied the outspray of water vapor and
244 axial shortening of the sample within the first 0.2 sec of each run. In contrast to the HVF
245 experiments, during the LVF experiments the frictional coefficient μ increased to 0.57
246 within a 2.5-sec period after 1 sec of the onset of slip, and gradually dropped to a
247 steady-state value of 0.28 prior to an elapsed time of ~20 sec, without distinct axial
248 shortening in the first 60 sec (Fig. 10c–d). This result indicates that slip weakening
249 occurred over a shorter period during the HVF experiments compared with the LVF
250 experiments.
251 During the HVF experiment, axial shortening occurred in the first 0.5 sec, and the
252 shortening amount decreased slightly from 0.025 to 0.02 mm over a period of 4.5 sec,
253 which corresponds to the onset of extrusion of molten run materials from the slip zone
254 (Fig. 10b). Significant shortening occurred continuously from 5 sec after the onset of

255 high-velocity slip (Fig. 10a), which corresponds to the period of extrusion of large
256 amount of molten run products from the slip zone (Fig. 4). In contrast, during the LVF
257 experiments, shortening occurred after 61 sec had passed since the initiation of slip (Fig.
258 10c–d).
259
260 ***3.5. FTIR and TG–DSC Analyses***
261
262 To quantitatively analyze the water contents of the starting rock sample and the run
263 products, we performed Fourier transform infrared (FTIR) and thermogravimetry
264 (TG)–differential scanning calorimetry (DSC) spectroscopic analyses using Jasco
265 FT/IR-300E and Netzsch STA 449C Jupiter apparatuses, respectively.
266 The run products of three HVF experiments (slip rate of 1.10 m/s and normal stresses
267 of 2, 5, and 9 MPa, respectively) were selected for FTIR analysis, which was performed
268 along profiles across the slip zone in thin sections of ~0.25 mm thick. In the FTIR
269 spectra, absorption bands are observed at the OH stretching region (3500–3700 cm^{-1}) in
270 the host serpentine sample but not in the slip zone ('run product' in Fig. 11). This result
271 indicates that little water (OH) remained in the slip zone. The water contents were
272 calculated using OH peaks at 3500–3700 cm^{-1} based on the method proposed by Beran
273 and Libowitzky [2006]. The calculated water contents are shown in Fig. 12.
274 The FTIR analyses show that no water occurs in the slip zone or in the adjacent
275 dehydration zones, and the water content ranges from 0.5 to 15 wt.% in the host rocks
276 (Fig. 12). These results indicate that all of the water in the slip zone and adjacent
277 dehydration zones (see Fig. 11) was released during the HVF experiments.

278 Four run products, of two HVF (1.10 m/s, No.1 and No.3) and two LVF (0.35 m/s,
279 MH001) experiments performed under normal stresses of 2.4–2.5 MPa, were powdered
280 for TG–DSC analysis. For comparison, one sample of host rock was also analyzed.
281 Approximately 30 mg of sample was placed in a covered $Pt_{90}Rh_{10}$ crucible and heated
282 from 25°C to 1050°C at a rate of 10°C min^{-1} under a flow of nitrogen gas (50 ml min^{-1}).
283 The DSC–TG spectra of the host rock sample reveal (i) a weight loss after heating of
284 6.9 wt.%, as determined by TG (Fig. 13a); and (ii) the heat flux during heating showed
285 an endothermic peak at 550–700°C and an exothermic peak at 800–850°C (Fig. 13b).
286 The first peak was accompanied by a weight loss, indicating that it corresponds to a
287 dehydroxylation reaction. The second peak was not accompanied by a weight loss, and
288 its relation to the reactions is currently unknown. The host sample was heated a second
289 time, from 25°C to 1050°C, showing no weight loss and no endothermic peak,
290 confirming that the dehydroxylation was completed during the first heating. The EPMA
291 analyses indicate marked differences in the analytical totals among the serpentine
292 minerals of the host rock (Table 2), the molten material remaining in the slip zone
293 (Table 3), and the dehydration zones (Table 4). The totals for the molten materials and
294 dehydration zones that abut the slip zone are up to 97–99.5 wt.%, about 9–11 wt.%
295 higher than that of the serpentine minerals of the host rock. Considering the presence of
296 ~35% olivine in the host rock sample, the differential amounts of 9–11 wt.% are
297 comparable to the weight loss of 6.9 wt.% in the run products, including molten
298 materials and fine-grained clasts of the host rock, as determined by TG (Fig. 13a).
299 Accordingly, the difference in analytical total reflects the release of water from the
300 molten materials and from serpentine minerals that abut the slip zone, due to the

301 dehydration of serpentine minerals.

302 Figure 13 shows the TG –DSC spectra of four run products, revealing that the total
303 weight losses of water are 0.0 wt.% for samples No. 1 and No. 3, 7.3 wt.% for MH001,
304 and 4.3 wt.% for MH002 (Fig. 14a). Samples No. 1 and No. 3 show no significant
305 endothermic peak at around 550–700°C (Fig. 14b), indicating that the dehydroxylation
306 reaction was completed in the HVF samples. In contrast, MH001 and MH002 show a
307 weight loss and an endothermic peak at around 550–700°C (Fig. 14b), similarly to the
308 host rock (Fig. 13b). This result suggests that the dehydroxylation reaction was not
309 completed during the LVF friction experiment at a low velocity of 0.35 m/s.

310

311 **4. Discussion and Conclusions**

312

313 ***4.1. Coseismic Melting and Dehydration Reaction***

314

315 The ejection of water vapor and the generation of vesicles within run products during
316 the HVF experiments provide conclusive proof that water was released from the slip
317 zone. The flow structures, the vitreous luster of run products (similarly to that of fresh
318 lava), and X-ray diffraction patterns indicate the coexistence of abundant fluid derived
319 from serpentine and frictional melt resulting from frictional heating in the slip zone. The
320 absence of antigorite crystals in the X-ray diffraction spectra of run products can be
321 interpreted as a result that antigorite crystals were completely broken down and/or
322 melted by friction heating.

323 As shown in Fig. 9, the molten materials have lower SiO_2 and Al_2O_3 components and

higher FeO component similar to that of olivine mineral contained in the host rock than that of serpentine mineral in the dehydration zone, and higher CaO and FeO components than that of serpentine contained in the host serpentinite. The FeO component of the molten materials is about 5~7 wt% higher than that of serpentine minerals contained in the host serpentinite and the dehydration zones, which is similar to that of olivine mineral contained in the host rock (Fig. 9). Furthermore, MgO and Al_2O_3 components of the molten materials are locally similar to that of olivine mineral, higher that of the host serpentine minerals contained in the host serpentinite and the dehydration zones (Fig. 9). These textural and petrologic features including the chemical compositions of molten materials reveal that the not only the serpentine but also the olivine minerals were melted by friction heating, and that a high temperature reached the bounding zones of the slip zone at which serpentine was involved in a dehydration reaction. Previous studies show that the high-velocity friction melting occurs in a chemically non-equilibrium process (Lin and Shimamoto, 1998; Lin, 2008) and that the melting or breakdown of serpentine mineral occurs at temperature of 400~600 °C [Spray, 1992]. Thus, the serpentine and olivine minerals are considered to be melted at temperature of ≥ melting points of these minerals. Based on the melting point (~1890 °C) of olivine [Spray, 1992], it is estimated that the temperature in the slip zone reached at least up to 1890 °C during the HVF experiments.

Previous studies indicate that the dehydration of serpentine occurs at temperature of ≥500°C [Ulmer and Trommsdorff, 1995; Viti, 2010] to 856°C [Lange and Ahrens, 1982]. In previous HVF experiments using marble samples, direct thermometer-based measurements of temperature indicate that the slip-zone temperature can reach

347 600–900°C during the first 0.1 sec of the experiment at a slip rate of 1.17 m/s [Han et al.,
348 2007]. TG, DTG and differential thermal analyzer (DTA) analyses show that serpentine
349 dehydration takes place between 550 and 800°C [Viti, 2010]. Calculation results for an
350 HVF experiment on serpentinite at a slip rate of 1.1 m/s reveal that the flash temperature
351 can rise by ~1250°C over a period of <0.1 sec [Hirose and Bystricky, 2007] and that the
352 temperature can reach 550–1100°C within a narrow slip zone (<3 mm wide) over a
353 period of 2–3 sec [Fukuchi and Imai, 2001]. Furthermore, seismic data reveal that if the
354 shear energy is constrained within 1 cm of the slip plane during seismic slip, the
355 temperature can readily increase to 100–1000°C during a medium- to large-magnitude
356 earthquake [Kanamori and Brodsky, 2004]. Thus, the temperature up to 1890°C in the
357 present HVF experiments as documented above, within a dehydration zone of <2 mm in
358 width (Fig. 12) and at slip rates of 1.10–1.31 m/s, is sufficient to induce the dehydration
359 of serpentine.
360 The breakdown of serpentine to olivine + talc + water and the breakdown of talc to
361 enstatite + quartz + water at 1 bar follow a second-order rate law [Bose and Ganguly,
362 1994]. The breakdown of antigorite in the present experiments is indicated by the
363 consumption of antigorite and increased integrated intensities of olivine in the X-ray
364 diffraction spectra for the run products, although talc could not be identified from the
365 spectra. Direct observations made during the present experiments also demonstrate that
366 serpentine dehydration reaction occurred within 0.2 sec of the onset of slip. Furthermore,
367 the antigorite crystals observed in the dehydration zones that abut the slip zone show
368 textural features indicative of decomposition, without the distinct cracks and fibrous
369 texture observed in the starting sample of host rock (Figs 5 and 6a–c). This finding

370 demonstrates that the serpentine dehydration reaction that occurred in a wide zone
371 involving the slip zone was caused mainly by the diffusion of frictional heat from the
372 slip zone. Our results support the idea that the diffusion of frictional heat is a major
373 coupling factor of thermal pressurization caused by the dehydration of serpentine within
374 seismogenic fault zone [Brantut et al., 2010].
375
376 ***4.2. Mechanism of Dynamic Weakening***
377
378 The dynamic weakening of faults during earthquakes is considered to result from
379 several mechanisms, including friction melting [Spray, 1993; Hirose and Shimamoto,
380 2005; Di Toro et al., 2006, 2011], the presence of S–C cataclasites [Lin, 1999, 2008],
381 the formation of fault gouge [e.g., Rice, 2006; Mizoguchi et al., 2007], thermal
382 pressurization [e.g., Lachenbruch and Sass, 1980; Wibberley and Shimamoto, 2005],
383 dehydration reactions involving water-rich minerals such as serpentine and kaolinite
384 [e.g., Hirose and Bystricky, 2007; Brantut et al., 2008; Viti and Hirose, 2010; Kohli et
385 al., 2011] as well as fault gouges present in seismogenic fault zones [e.g., Famin et al.,
386 2008; Hamada et al., 2009, 2011], thermal decomposition [Han et al., 2007], and the
387 dehydroxylation of mica minerals [Hirono and Tanikawa, 2011]. Each of these
388 mechanisms is closely linked to frictional heating generated upon the fault plane during
389 seismic slip. The frictional melt generated in the slip zone also plays an important role
390 in lubricating the slip plane, thereby facilitating further slip along seismogenic faults
391 during large earthquakes [e.g., Di Toro et al., 2006, 2011]. Although dynamic fault
392 strength during frictional melting is commonly considered to be controlled by the

393 development of a molten layer and by the viscosity of this layer [Spray, 1993; Hirose
394 and Shimamoto, 2005], the serpentinite dehydration may also be a main mechanism
395 resulting in a dramatic increase in pore pressure that may lead to the dynamic weakening
396 of seismogenic faults. The outspray of water vapor within the first 0.2 sec of each run as
397 observed during the HVF experiments indicates that the dehydration of serpentine
398 occurred in the first 0.2 sec. The fact that molten materials were squeezed out after 0.5
399 sec after the onset of the slip from the slip zone as observed during the experiments
400 reveals that a molten layer was produced in the same time as the water vapor within the
401 slip zone during the first 0.5 sec. These findings indicate that both water vapor and
402 molten material were co-existed in the slip zone in the first 0.5 sec of the run. It may be
403 difficult to produce sufficient fault gouge material to affect the fault strength over a
404 short duration of 0.2 sec because of small amount of generated slip. Accordingly, the
405 dramatic decrease in the frictional coefficient from 0.56 to 0.25 in the first 0.2 sec after
406 the onset of slip (Fig. 10a–b) can be interpreted as a result of thermal pressurization
407 caused by the dehydration of serpentine that accompanies frictional melting during the
408 HVF experiments. In contrast, similar weakening was observed in the LVF experiments,
409 in which the frictional coefficient decreased from 0.55 to 0.25, but this took ~10 sec
410 after the onset of run (Fig. 10c–d). This may be interpreted as that enough amount of
411 fine-grained material (fault gouge) formed in the slip zone which weakened the fault
412 strength as proposed by previous studies [Rice, 2006; Mizoguchi et al., 2007].
413 In the present study, it is considered that the main weakening mechanism of the
414 simulated faults under conditions equivalent to large earthquake slip was the thermal
415 pressurization caused by serpentine dehydration associated with frictional heating and

416 melting, resulting in the excess saturation pressure of water vapor and fluid including
417 melt in the slip zone. Previous studies show that frictional heating would cause the fluid
418 in the fault gouge to expand in volume much more than would be the solid cage [e.g.,
419 Sibson, 1973, Lachenbruch and Sass, 1980]. Thus, shear-induced dilatancy of the gouge
420 overwhelms the thermal expansion effect and a pressure increased must be induced in
421 the pore pressure [Rice and Cocco, 2007]. The saturation pressure of water vapor is
422 known to vary with the temperature of the vapor [Kaye and Laby, 1986]: when confined
423 water is heated, the saturation pressure of water vapor (P) shows a rapid increase.
424 Assuming ideal gas (water vapor) behavior, $P = nRT/V$, where n is the number of moles,
425 R is the water vapor constant, T is absolute temperature (K), and V is the volume of
426 water vapor. From room temperature (20°C) to 360°C, P increases by three orders of
427 magnitude, from ~10^{-2} to ~20 MPa [Kaye and Laby, 1986]. Theoretically, under the
428 pressure–temperature conditions of seismogenic depths, the thermal expansivity of
429 water is on the order of 10^{-3}/°C, meaning that the increase in fluid pressure at the depths
430 of hypocenters would be on the order of 1 MPa/°C [Lachenbruch and Sass, 1980;
431 Kanamori and Brodsky, 2004]. Thus, the corresponding pressure of water vapor and
432 fluid would be >20 MPa in a simulated fault zone under conditions equivalent to large
433 earthquake slip, comparable to the stress drop that occurs during large earthquakes
434 [O'Hara et al., 2006]. In the present HVF experiments, the decrease in the average
435 shortening amount in the first 5 sec after the onset of slip can be interpreted as a result
436 of pore pressure increase due to the thermal pressurization that accompanies frictional
437 melting within the slip zone. The subsequent increase in the average shortening amount
438 could reflect the extrusion of run products (including vapor, melt, and fine-grained

439 materials) from the slip zone, as shown in Fig. 4.

440 Our results support the idea that the thermal pressurization of fluid released by the
441 dehydration of serpentine and friction melt plays an important role in the dynamic
442 weakening of faults during seismic slip within seismogenic fault zones.

443

444 ***4.3. Tectonic Implications***

445

446 The present experimental results have significant implications for subduction zone
447 earthquakes and transform faults such as the San Andreas Fault. Seismogenic faults
448 within a subduction zone are generally associated with a mantle wedge composed of
449 serpentinites that contain ~13 wt.% H_2O [Ulmer and Trommsdorff, 1995]. Hydrous
450 antigorite may play an important role in the transport of water into the earth when it
451 enters a subduction zone. The present results show that the frictional heat generated
452 upon a seismogenic slip plane under conditions of large earthquake slip can lead to
453 melting in a seismic slip zone and the dehydration of serpentinite within a wide
454 dehydration reaction zone (comprising the main slip zone and bounding zones) due to
455 the diffusion of frictional heat from the slip plane, thereby increasing the pore pressure
456 due to the thermal expansivity of fluid and water vapor. Furthermore, the frictional melt
457 generated in the slip zone also plays an important role in lubricating the slip plane,
458 facilitating further slip along seismogenic faults during large earthquakes (Di Toro et al.,
459 2011). Accordingly, our experiment results confirm that the serpentine dehydration that
460 accompanies frictional melting results in a sudden increase in pore pressure, which in
461 turn may lead to a reduction in the effective normal stress across the fault, in turn

462 resulting in a marked reduction in the dynamic fault strength, thereby enabling further
463 slip along the fault in a subduction zone.
464 This sequence of events might also influence the physics of earthquake processes
465 within subduction zones, explaining the large seismic slip of >15–50 m generated by
466 huge subduction-zone earthquakes such as the 2004 M_w 9.4 Sumatra–Andaman
467 earthquake [Subarya et al., 2006] and the 2011 M_w 9.1 Tohoku Japan earthquake [Yagi
468 and Fukahata, 2011]. In addition, if the large volumes of fluid released by the
469 dehydration of serpentinites during huge earthquakes are concentrated upon and migrate
470 along pre-existing fault zones to neighboring fault segments, such a sudden increase in
471 fluid pressure would promote further brittle failure in barrier areas of seismogenic faults
472 and in neighboring fault segments. The present results indicate that the dynamic
473 parameters of seismogenic faults are strongly affected by serpentine dehydration during
474 large earthquakes within subduction zones and along intracontinental faults that contain
475 abundant hydrous minerals.
476
477 **Acknowledgments**
478
479 We are grateful to Prof. T. Shimamoto for designing the rotary-shear low- to
480 high-velocity test machine. This work was supported by a Grand-in-Aid for Scientific
481 Research (Science Project No. 23253002 for A. Lin) from the Ministry of Education,
482 Culture, Sports, Science and Technology of Japan.
483

484 **References**

485

486 Andrews, D. J., 2002. A fault constitutive relation accounting for thermal pressurization
487 of pore fluid. J. Geophys. Res. 107, B001942, doi:10.1029/2002J.

488 Beran, A., Libowitzky, E., 2006. Water in natural mantle minerals II: olivine, garnet
489 and accessory minerals. Reviews in Mineralogy and Geochemistry, 62, 169–191.

490 Bose, K., Ganguly, J., 1994. Thermogravimetric study of dehydration kinetics of talc.
491 Am. Mineral. 79, 692-699.

492 Brantut, N., Schubnel, A., Rouzaud, J.-N., Brunet, F., Shimamoto , T., 2008. High
493 velocity frictional properties of a clay-bearing fault gouge and implications for
494 earthquake mechanics. J. Geophys. Res. 113, B10401, doi:10.1029/2007JB005551.

495 Brantut N., Schubnel, A., Corvisier, J., Sarout, J., 2010. Thermochemical pressurization
496 of faults during coseismic slip. J. Geophys. Res. 115, B05314,
497 doi:10.1029/2009JB006533.

498 Brantut, N., Han, R., Shimamoto, T., Findling, N., Schubnel, A., 2011. Fast slip with
499 inhibited temperature rise due to mineral dehydration: Evidence from experiments
500 on gypsum. Geology 39, 59–62.

501 Christensen, N. J., 1972. The abundance of serpentinites in the oceanic crust. J. Geophys.
502 Res. 80, 709–719.

503 Di Toro, G., Goldsby, D. L., Tullis, T. E., 2006. Friction falls towards zero in quartz
504 rock as slip velocity approaches seismic rates. Nature 427, 436–439.

505 Di Toro, G., Han, R., Hirose, T., De Paola, N., Nielsen, S., Mizoguchi, K., Ferri, F.,
506 Cocco, M., Shimamoto, T., 2011. Fault lubrication during earthquakes, Nature, 471,

494-498.

Famin, V., Nakashima, S., Boullier, A.-M., Fujimoto, K., Hirono, T., 2008. Earthquake produce carbon dioxide in crustal faults. Earth and Planetary Sci. Lett. 265, 487–497.

Francis, T. J. G., 1981. Serpentinization faults and their role in the tectonics of slow spreading ridges. J. Geophys. Res. 86, 11616-11622.

Fukuchi, T., Imai, N., 2001. ESR and ICP analyses of the DPRI 500 m drill core samples penetrating through the Nojima Fault, Japan. Island Arc 10, 465– 478.

Goldsby, D.L., Tullis, T., 2011. Flash heating leads to low frictional strength of crustal rocks at earthquake slip rates. Science 334, 216–218.

Hamada, Y., Hirono, T., Tanikawa, W., Soh, W., Song, S., 2009. Energy taken up by co-seismic chemical reactions during a large earthquake: An example from the 1999 Taiwan Chi-Chi earthquake. Geophys. Res. Lett. 36, L06301, doi:10.1029/2008GL036772.

Hamada, Y., Hirono, T., Ishikawa, T., 2011. Coseismic frictional heating and fluid-rock interaction in a slip zone within a shallow accretionary prism and implications for earthquake slip behavior. J. Geophys. Res. 116, B01302, doi:10.1029/2010JB007730.

Han, R., Shimamoto, T., Hirose, T., Ree, J.-H., Ando J., 2007. Ultra-low friction of carbonate fault caused by thermal decomposition. Science 316, 878–881.

Han, R., T. Hirose, Shimamoto, T., 2010. Strong velocity weakening and powder lubrication of simulated carbonate faults at seismic slip rates. J. Geophys. Res. 115, B03412, doi:10.1029/2008JB006136.

530 Hirono, T., Tanikawa, W., 2011. Implications of the thermal properties and kinetic
531 parameters of dehydroxylation of mica minerals for fault weakening, frictional
532 heating, and earthquake energetics. Earth and Planetary Sci. Lett. 307, 161–172.
533 Hirono, T., Fujimoto, K., Yokohama, K., Hamada, T., Tanikawa, W., Tadai, O.,
534 Mishima, T., Tanimizu, M., Lin, W., Soh, W., Song, S., 2008. Clay mineral
535 reactions caused by frictional heating during an earthquake: An example from the
536 Taiwan Chelungpu fault. Geophys. Res. Lett., 35, L16303,
537 doi:10.1029/2008GL034476.
538 Hirose, T., Shimamoto, T., 2005. Growth of molten zone as a mechanism of slip
539 weakening of simulated faults in gabbro during frictional melting. J. Geophys. Res.
540 110, B05202, doi:10.1029/2004JB003207.
541 Hirose, T., Bystricky, M., 2007. Extreme dynamic weakening of faults during
542 dehydration by coseismic shear heating. Geophys. Res. Lett. 34, L14311,
543 doi:10.1029/2007GL030049.
544 Kanamori, H., Brodsky, E. E., 2004. The physics of earthquake, Rep. Prog. Phys. 67,
545 1429–2496.
546 Kaye, G.W.C., Laby, T. H., 1986. Tables of physical and chemical constants. John
547 Willey and Sons Inc., New York, 432p.
548 Kohli, A.H., Goldsby, D. L., Hirth, G., Tullis, T., 2011. Flash weakening of serpentinite
549 at near-seismic slip rates. J. Geophys. Res. 116, B03202,
550 doi:10.1029/2010JB007833
551 Lachenbruch, A. H., and J. H. Sass (1980), Frictional heating, fluid pressure, and the
552 resistance to fluid motion. J. Geophys. Res., 85, 6185–6222.

553 Lange, M. A., Ahrens, T. J., 1982. Impact induced dehydration of serpentine and the
554 evolution of planetary atmospheres, J. Geophys. Res. 87, A451–A456.
555 Lin, A., 1994. Glassy pseudotachylyte veins from the Fuyun fault zone, northwest China.
556 J. Struct. Geol. 16, 71–83.
557 Lin, A., 1999. S-C cataclasite in granitic rocks. Tectonophysics 304, 257–273.
558 Lin, A., 2002. Co-seismic strike-slip and rupture length produced by the Ms 8.1 Central
559 Kunlun earthquake. Science 296, 2015–2017.
560 Lin, A., 2008. Fossil earthquakes: the formation and preservation of pseudotachylytes.
561 Springer, Berlin, 348p.
562 Lin, A., Shimamoto, T., 1998. Selective melting processes as inferred from
563 experimentally-generated pseudotachylytes,. J. Asian Earth Sci. 16, 533–545.
564 Maddock, R. H., Grocott, J., Van Nes, J., 1987. Vesicles, amygdales and similar
565 structures in fault-generated pseudotachylytes. Lithos 20, 419–432.
566 Magloughlin, J. F., 2011. Bubble collapse structure: a microstructural record of fluids,
567 bubble formation and collapse, and mineralization in pseudotachylyte. Journal of
568 Geology 119, 351–371.
569 Meade, C., Jeanloz, R., 1991. Deep focus earthquake and recycling of water into the
570 Earth' mantle. Science 252, 68–72.
571 Mizoguchi, K., Hirose, T. Shimamoto, T., Fukuyama, F., 2007. Reconstruction of
572 seismic faulting by high-velocity friction experiments: An example of the 1995
573 Kobe earthquake. Geophys. Res. Lett. 34, L01308, doi: 10.1029/2006GL027931.
574 Moore, D. E., Rymer, M.J., 2007. Talc-bearing serpentinite and the creeping section of
575 the San Andreas fault. Nature 448, 795–797.

576 O'Hara, K. D., Mizoguchi, K., Shimamoto, T., Hower, J., 2006. Experimental frictional
577 heating of coal gouge at seismic slip rates: Evidence for devolatilization and
578 thermal pressurization of gouge fluids.Tectonophysics 424, 109–118.
579 Rice, J. R., 2006. Heating and weakening of faults during earthquake slip. J. Geophys.
580 Res. 110, B05311, doi: 10.1029/2005J B004006.
581 Shimamoto, T., Tsutsumi, A., 1994. A new rotary-shear high-speed frictional testing
582 machine: its basic design and scope of research. Structural Geology, The Journal of
583 Tectonic Group Japan 39, 65–78 (in Japanese with English abstract).
584 Sibson, R., 1973. Interactions between temperature and pore-fluid pressure during
585 earthquake faulting and a mechanism for partial or total stress relief. Nature 243,
586 66–68.
587 Spray, J., 1992. A physical basis for the frictional melting of some rock-forming
588 minerals. Tectonophysics 204, 2205–221.
589 Spray, J., 1993. Viscosity determination of some fractionally generated silicate melts:
590 implication for fault zone rheology at high strain rates. J. Geophys. Res. 98,
591 8053–8068.
592 Subarya, C., Chlieh, M., Prawirodirdjo, L., Avouac, J., Bock, Y., Sieh, K., Meltzner,
593 A.J., Natawidjaja, D.H., R. McCaffrey, R., 2006. Plate-boundary deformation
594 associated with the great Sumatra-Andaman earthquake. Nature 440, 46–51.
595 Tibi, R., G. Rock, Estabrook, C.H., 2002. Seismic body wave constraint on mechanisms
596 of intermediate-depth earthquakes. J. Geophys. Res. 107,
597 doi:10.1029/200JB000361.
598 Ulmer, P., Trommsdorff, V., 1995. Serpentine stability to mantle depths and

599 subduction-related magmatism. Science 268, 858–861.
600 Viti, C., 2010. Serpentine minerals discrimination by thermal analysis. American
601 Mineralogist 95, 631–638.
602 Viti, C., Hirose, T., 2010. Thermal decomposition of serpentine during coseismic
603 faulting: Nanostructures and mineral reactions. J. Struct. Geol. 32, 1476-1484.
604 Wibberley, C. A. J., 2007. Seismology: Talc at fault. Nature 448, 756–757.
605 Wibberley, C. A. J., Shimamoto, T., 2005. Earthquake slip weakening and asperities
606 explained by thermal pressurization. Nature 436, 689–692.
607 Yagi, Y., Fukahata, Y., 2011. Rupture process of the 2011 Tohoku-oki earthquake and
608 absolute elastic strain release. Geophys. Res. Lett. 38, L19307,
609 doi:10.1029/2011GL048701.
610

611 **Captions to figures**

612 Figure 1. Diagram showing the rotary-shear low- to high-velocity frictional testing
613 machine equipped with a hydraulic pressure vessel. 1: specimen holder (one-axis
614 rotary-shear specimen box); 2: pressure vessel for elevated pore-water pressure;
615 3–4: torque and axial force gauges; 4: electromagnetic clutch; 5: force gouge; 6:
616 oil pressure cylinder; 7: servo-motor and gear system; 8: motor controller; 9:
617 manual pump; 10: oil pressure pump; 11–12: manual oil pressure pump; 13:
618 pressure generator system; 14–15: data recording system. This machine was
619 installed at Shizuoka University, Japan, in early 2007.

620 Figure 2. Close-up view of the specimen holder (a), configuration of the specimen set (b),
621 and orientation of the thin section cut from the run products (c). The thin section is
622 oriented perpendicular to the slip zone.

623 Figure 3. Petrographic features of serpentinite used for the frictional experiments in this
624 study. (a) Photomicrograph (cross polarized light); (b) scanning electron image.
625 The serpentinite is composed of 65% serpentine (antigorite) and 35% olivine.

626 Figure 4. Photographs taken through the transparent window cover of the experimental
627 apparatus showing dust and water vapor (a, c, d), and sparks of yellow–red melt (b)
628 ejected from the interface (slip zone) of two cylindrical serpentinite specimens at a
629 slip rate of 1.10 m/s and normal stress of 6.5 MPa during a high-velocity friction
630 (HVF) experiment (HVF R001). The water vapor cooled to form water droplets
631 (Wd) upon the window cover along a zone of 2–7 mm in width during the 20 sec
632 duration of the experiment.

633 Figure 5. Photomicrograph (a) and back-scattered electron micrograph (b) showing

representative microstructures of a simulated fault zone (slip zone) in a high-velocity friction (HVF) experiment (run HVF R001) conducted at a slip rate of 1.10 m/s. Note that dehydrated zones (dz) are developed on both sides of the slip zone.

Figure 6. Back-scattered electron micrographs showing representative microstructures of a simulated fault zone (slip zone) in experiment run HVF R001 conducted at a slip rate of 1.10 m/s, showing (a) the slip zone and dehydration zone (dz); (b) a close-up view of the dehydrated zone in serpentine; (c) a close-up view of (b); and (d) representative textures of run products ejected from the slip zone, showing melt textures and flow layers, vesicles (v), and a fine-grained matrix (molten material).

Figure 7. Representative textures of run products. (a) Photograph of fine-grained matrix (molten material) ejected from the slip zone, showing flow textures, vesicles, and a vitreous luster similar to that of fresh lava. (b) Back-scattered electron micrograph showing the textures of vesicles and fine-grained clasts (HVF R001 run product).

Figure 8. Powder X-ray diffraction spectra derived from (a) the host serpentinite, (b) reference olivine, and (c–f) representative run products remaining in the slip zone, for experiments with a slip rate of 1.31 m/s and normal stress of 5 MPa (run HVF R012) (c), and a slip rate of 1.10 m/s and normal stress of 6.5 MPa (run HVF R001) (d). The sample (HVF 012) was picked from the run product material extruded from the slip zone, and the sample (HVF R001) was separated from the run product remained in the slip zone. (e) Enlargement of (d) between 2θ values of 15° and 35°, and (f) calibrated sample containing 90 wt.% fine-grained clasts of run product and 10 wt.% glass (obsidian). ol: olivine; ant: antigorite. Note that the

run product (HVF R001) showed a distinct, broad range of 2θ values from 20° to 35°, as observed for the calibrated sample containing 10 wt.% glass (f). The vertical axis (diffraction density) is the same for all spectra. CPS: counts per second.

Figure 9. Variation of major oxides in the host serpentinite, slip zone and dehydration zone generated in the HVF experiments. Data are shown in Tables 2-4.

Figure 10. Friction coefficient versus time for experiment run HVF R012 at a slip rate of 1.31 m/s and normal stress of 5 MPa (a–b), and run LVFR110 at a slip rate of 0.35 m/s and normal stress of 8 MPa (c–d). (b) Enlargement of the first 2.4 sec of the HVF experiment shown in (a). (d) Enlargement of the first 20 sec of the LVF experiment shown in (c).

Figure 11. Representative FTIR spectra of the host rock (serpentinite) and run product of a high-velocity friction experiment (MH R0012). Note that the OH peaks are present at 3500–3700 cm^{-1} in the host serpentine sample but not in the slip zone.

Figure 12. Water contents of the high-velocity friction (HVF) run products calculated from the Fourier transform infrared (FTIR) spectra. Note that the narrow and wide zones reflect a change in slip zone width, as shown in Figs 5 and 6.

Figure 13. Thermogravimetry–differential scanning calorimetry (TG–DSC) spectra of the host rock (serpentinite). (a) TG, (b) DSC. Note that the heat flux during the heating showed an endothermic peak at 550–700°C and an exothermic peak at 800–850°C.

Figure 14. Thermogravimetry–differential scanning calorimetry (TG–DSC) spectra of the run products of high-velocity friction (HVF) experiments (No. 1 and No. 2),

680 and low-velocity friction (LVF) experiments (MH001 and MH002). (a) TG, (b)

681 DSC. See the text for details.

682

Figure1

Click here to download high resolution image

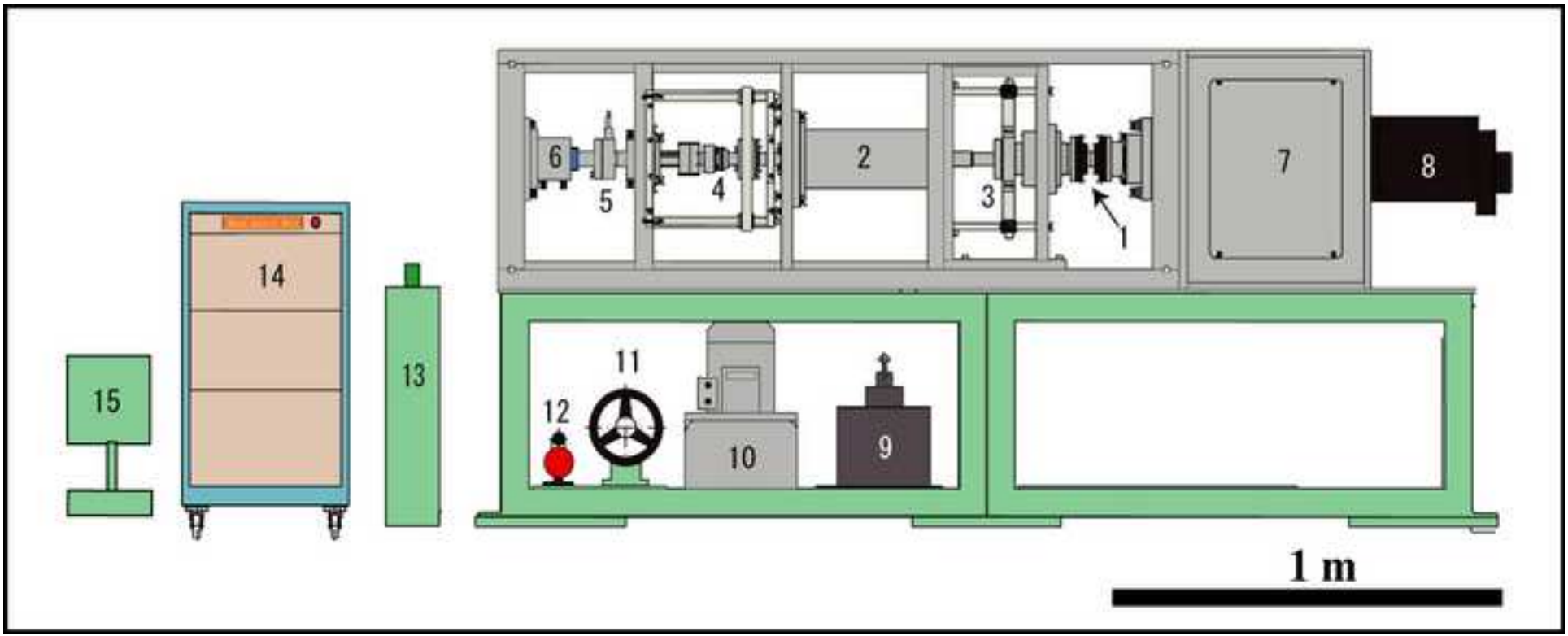

Figure2

Click here to download high resolution image

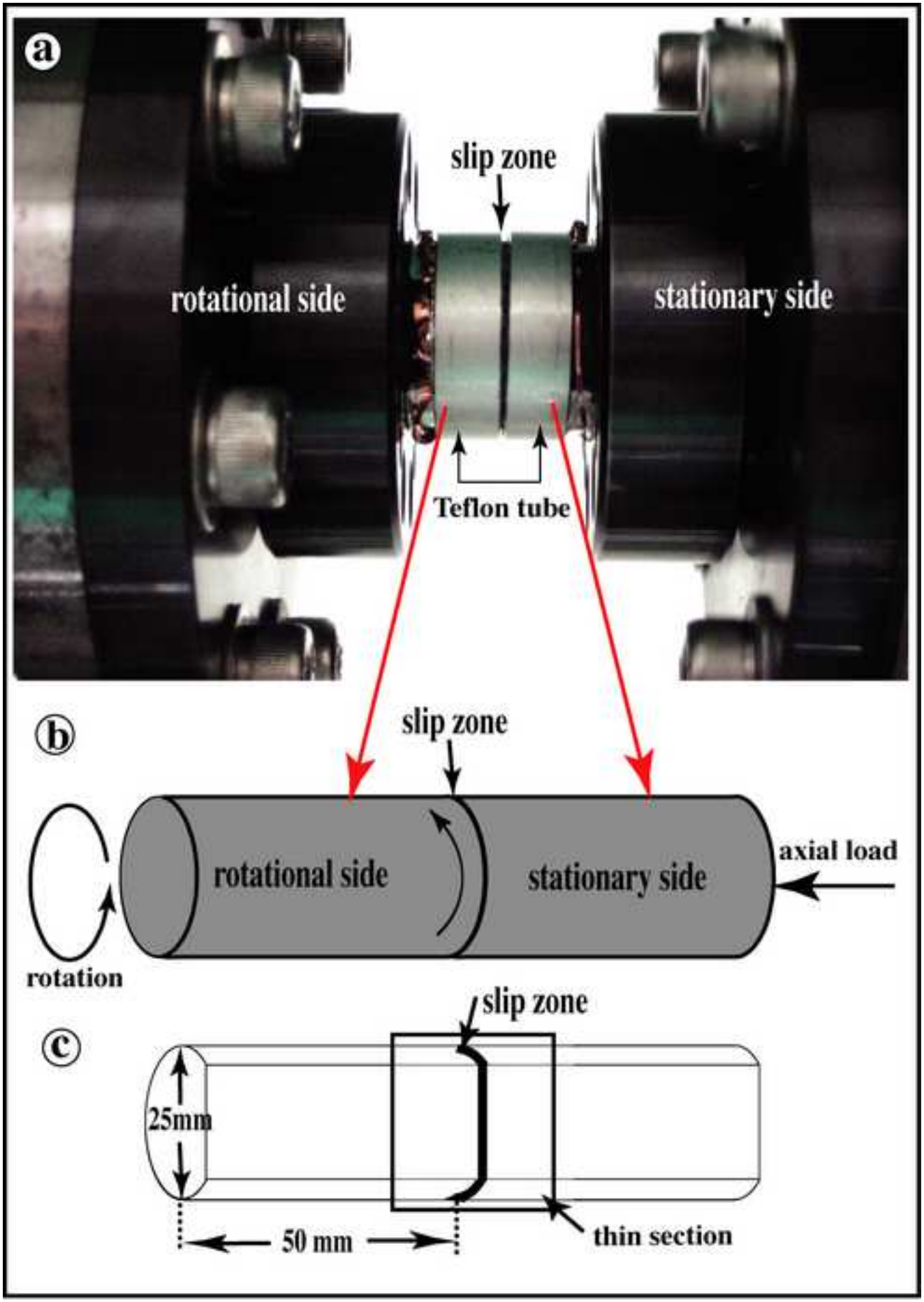

Figure3

Click here to download high resolution image

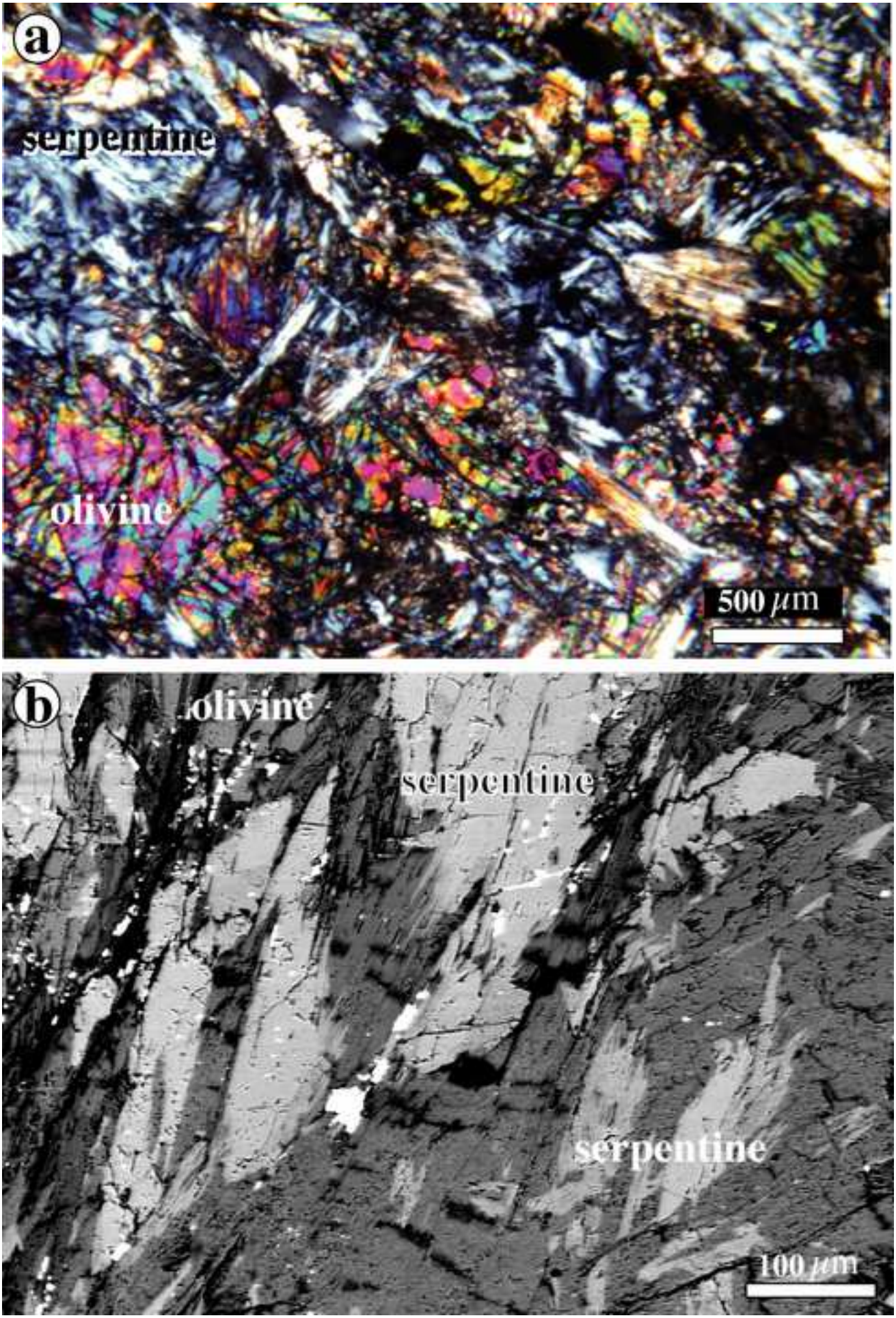

Figure4

Click here to download high resolution image

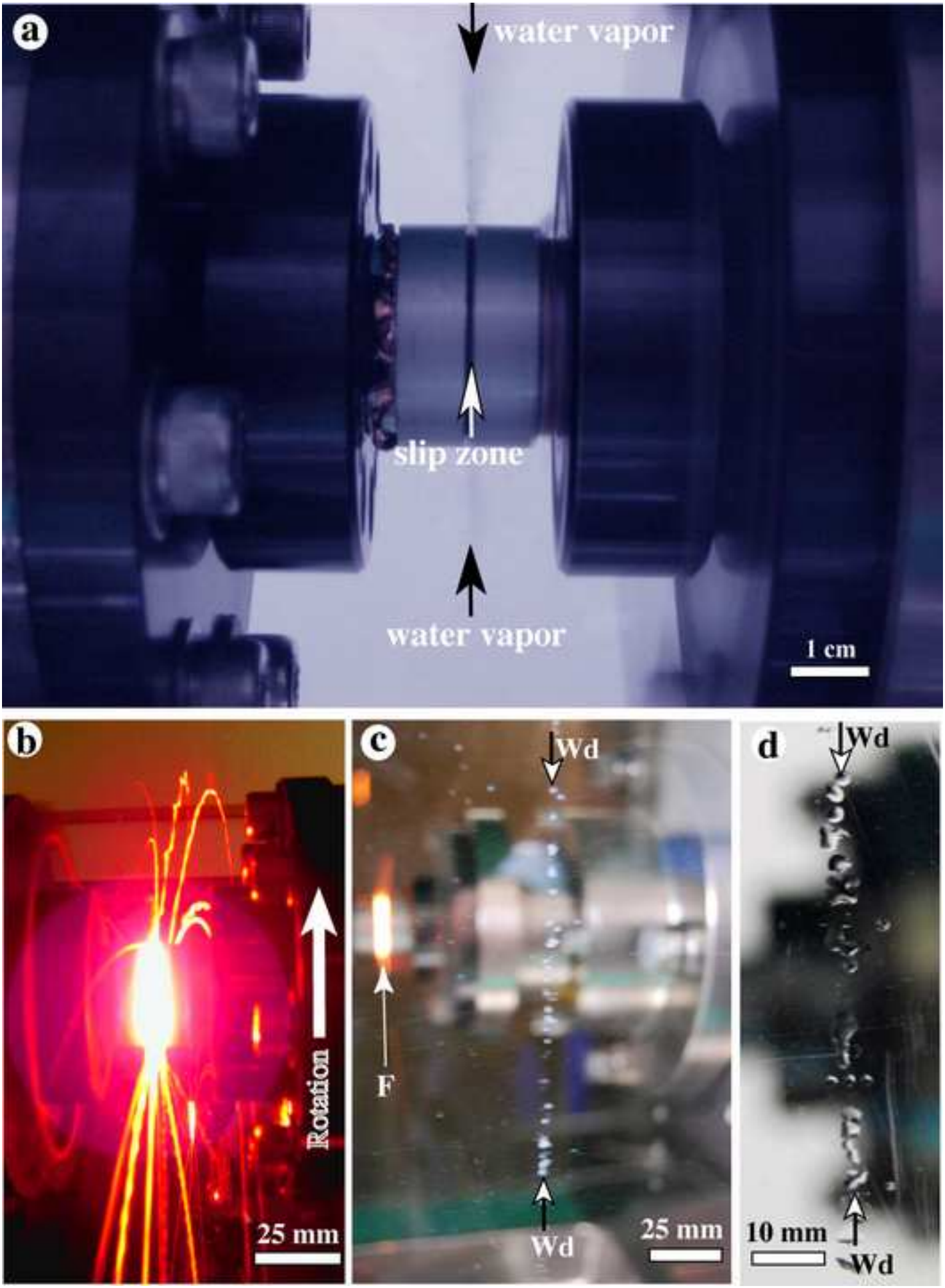

Figure5

Click here to download high resolution image

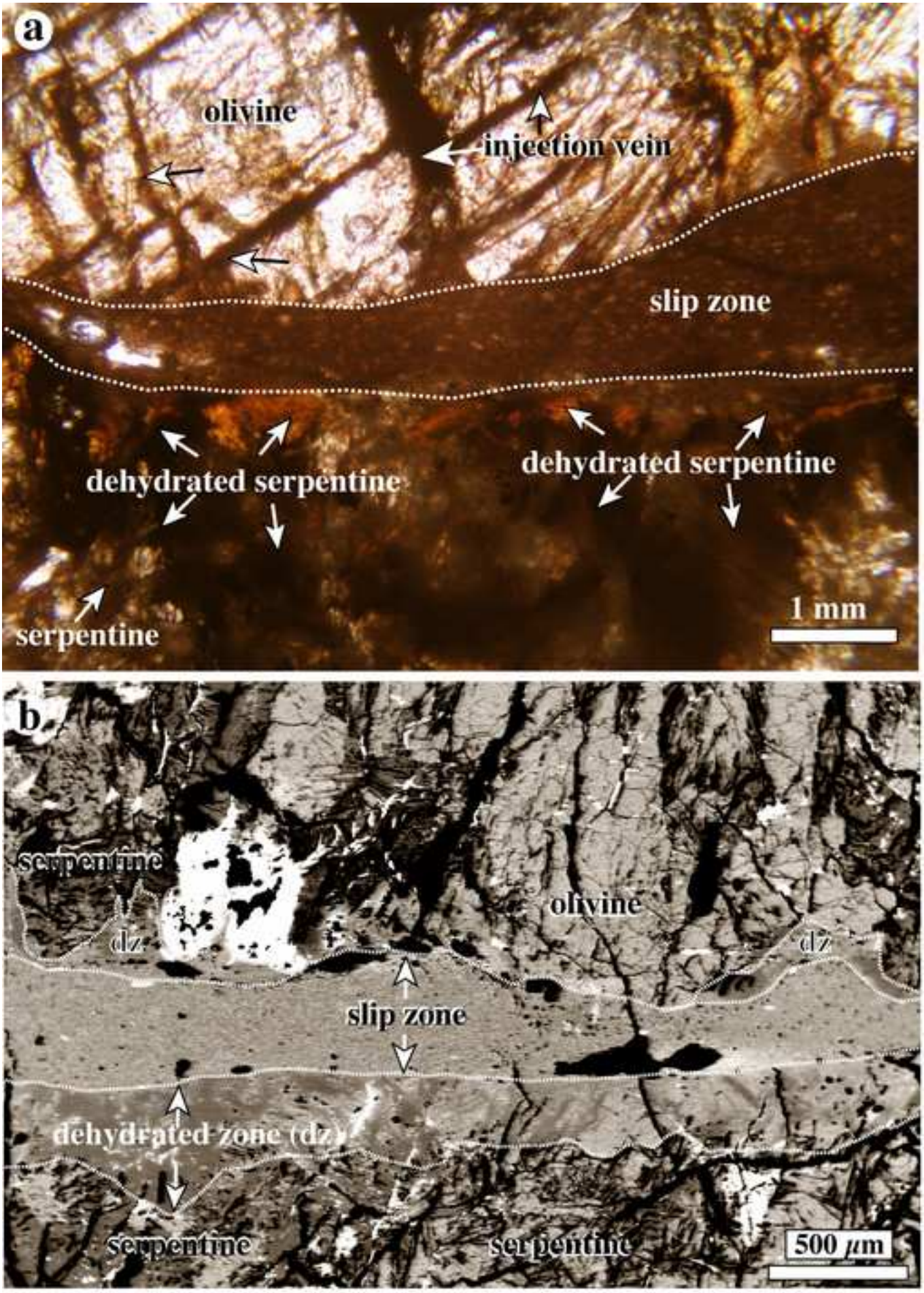

Figure6

Click here to download high resolution image

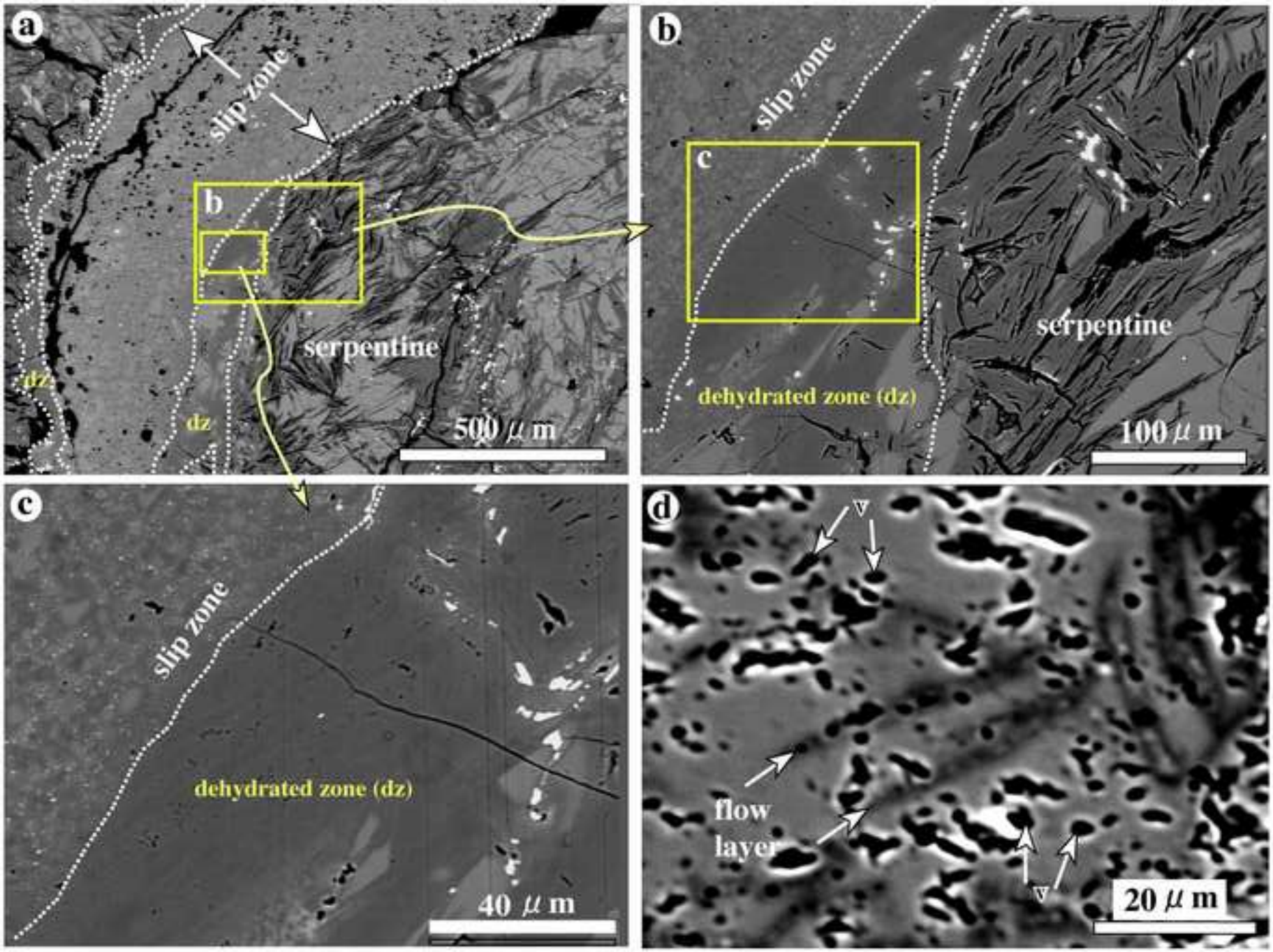

Figure7

Click here to download high resolution image

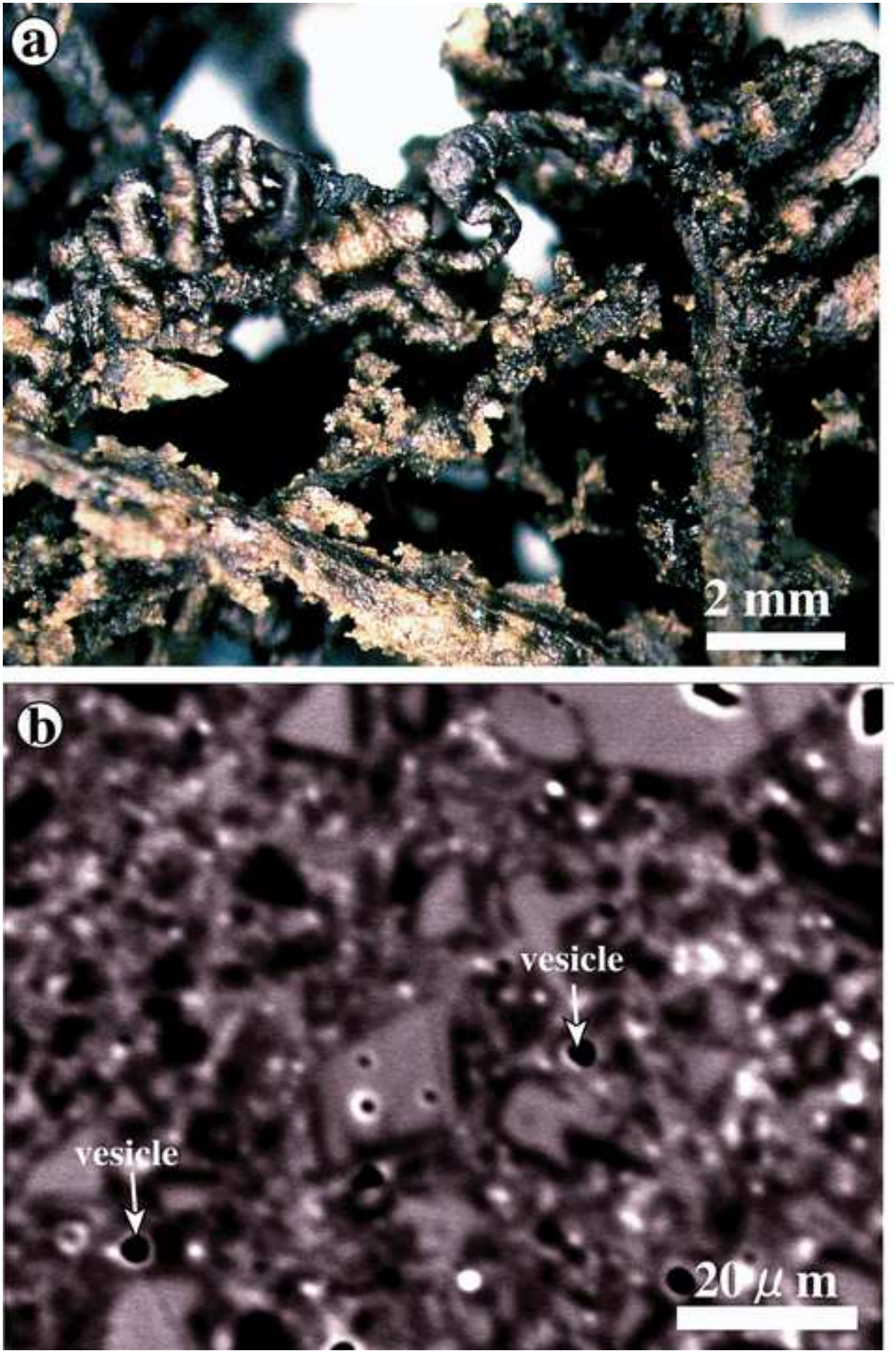

Figure8

Click here to download high resolution image

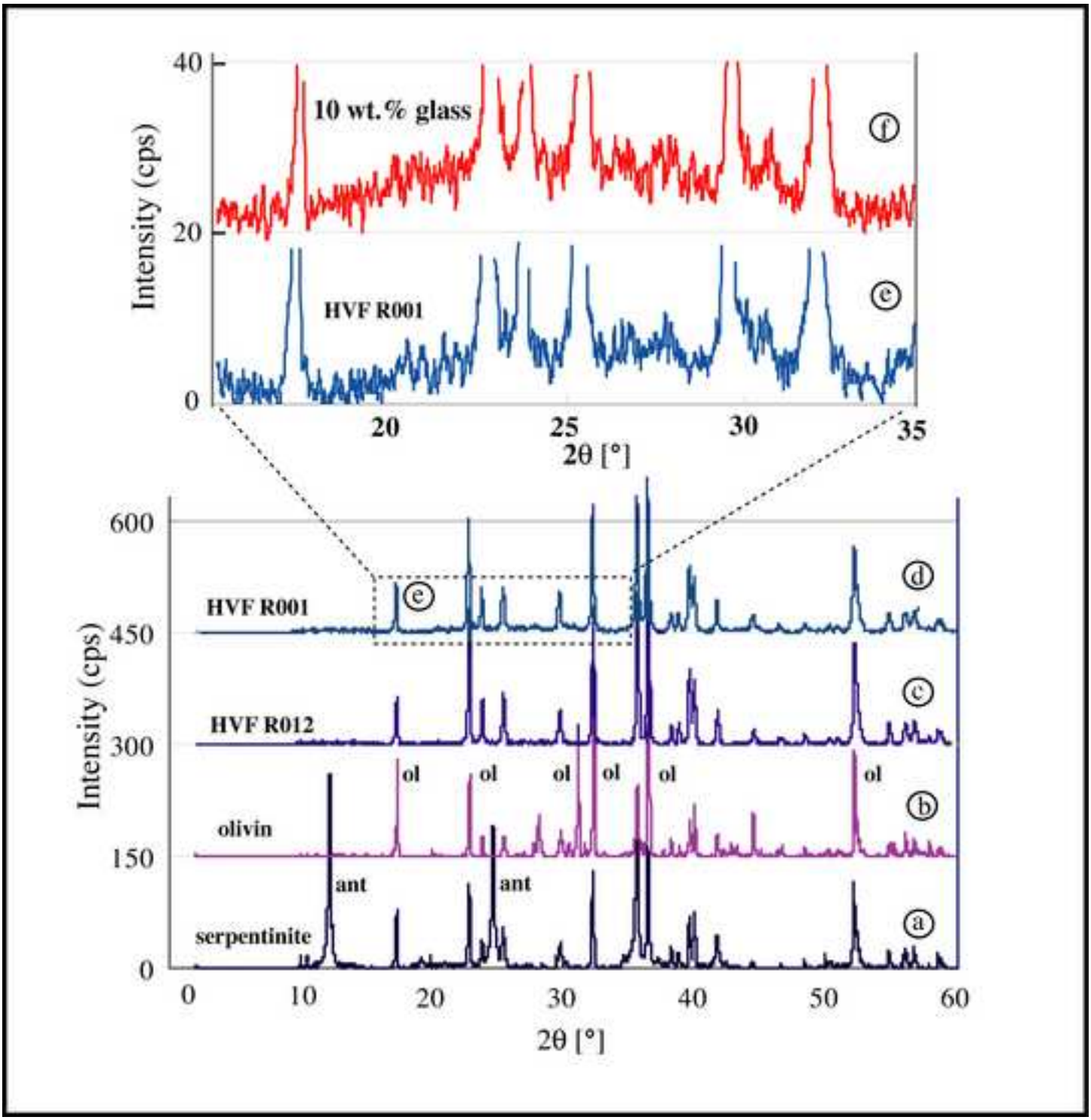

Figure9

Click here to download high resolution image

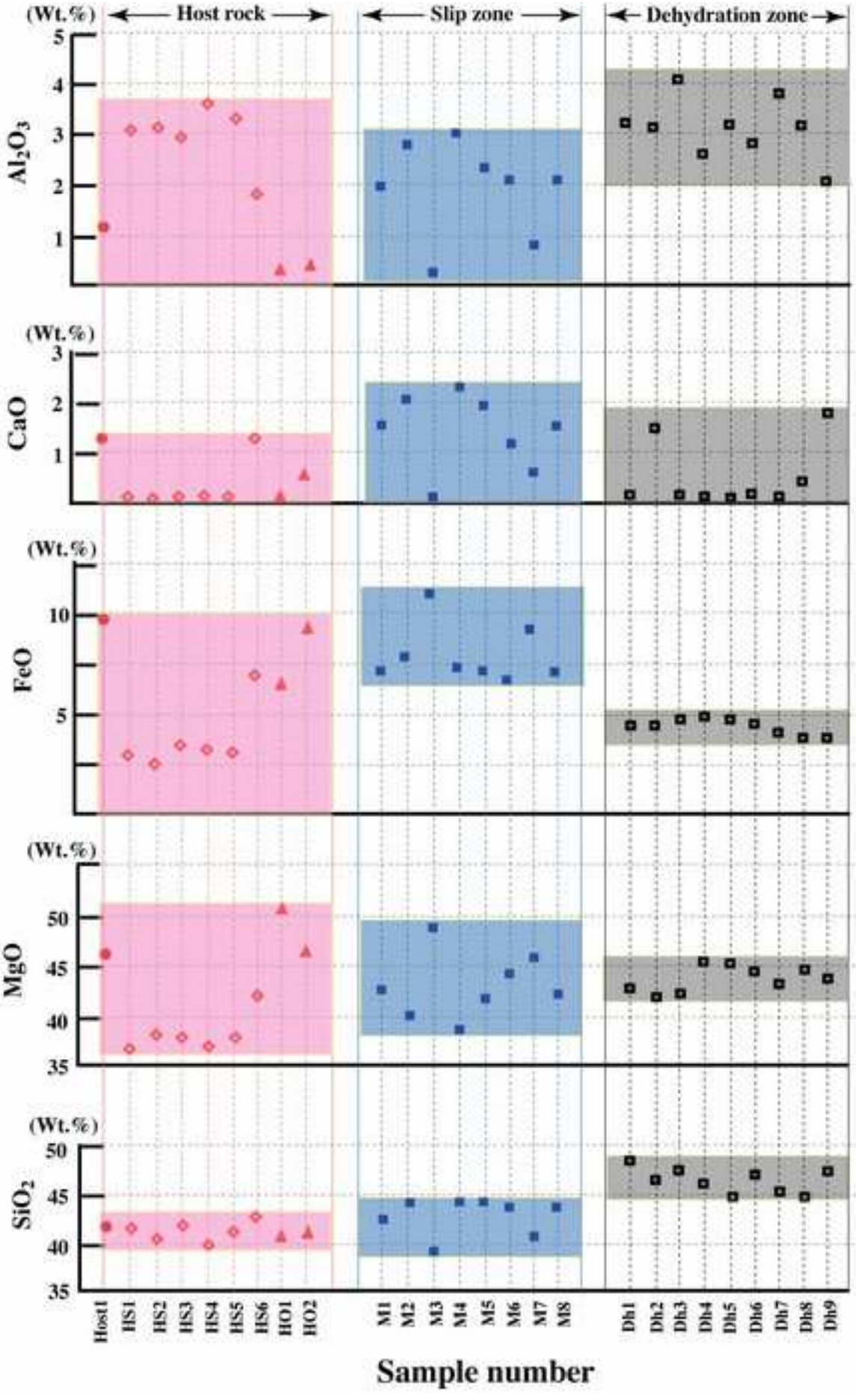

Figure10

Click here to download high resolution image

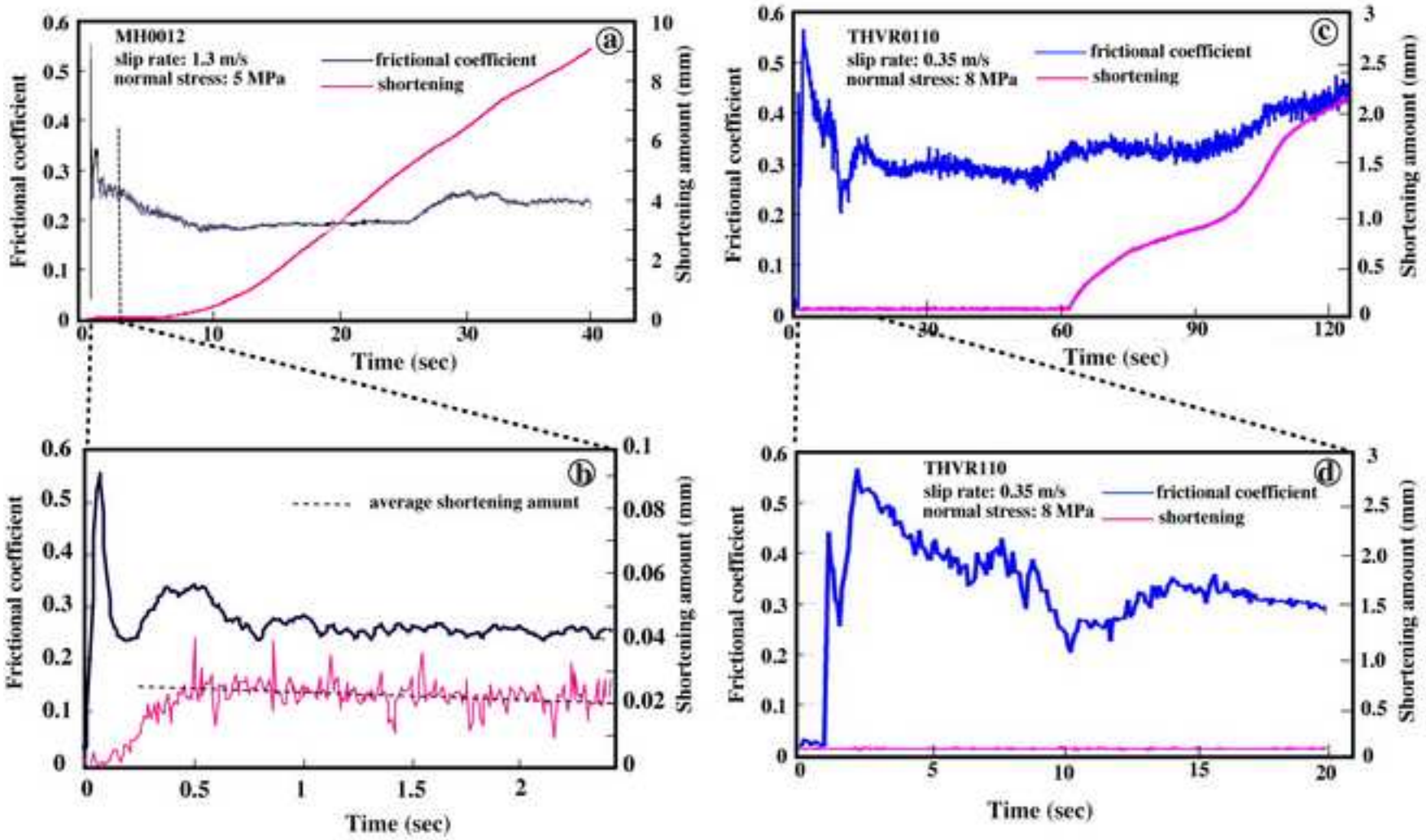

Figure11
Click here to download high resolution image

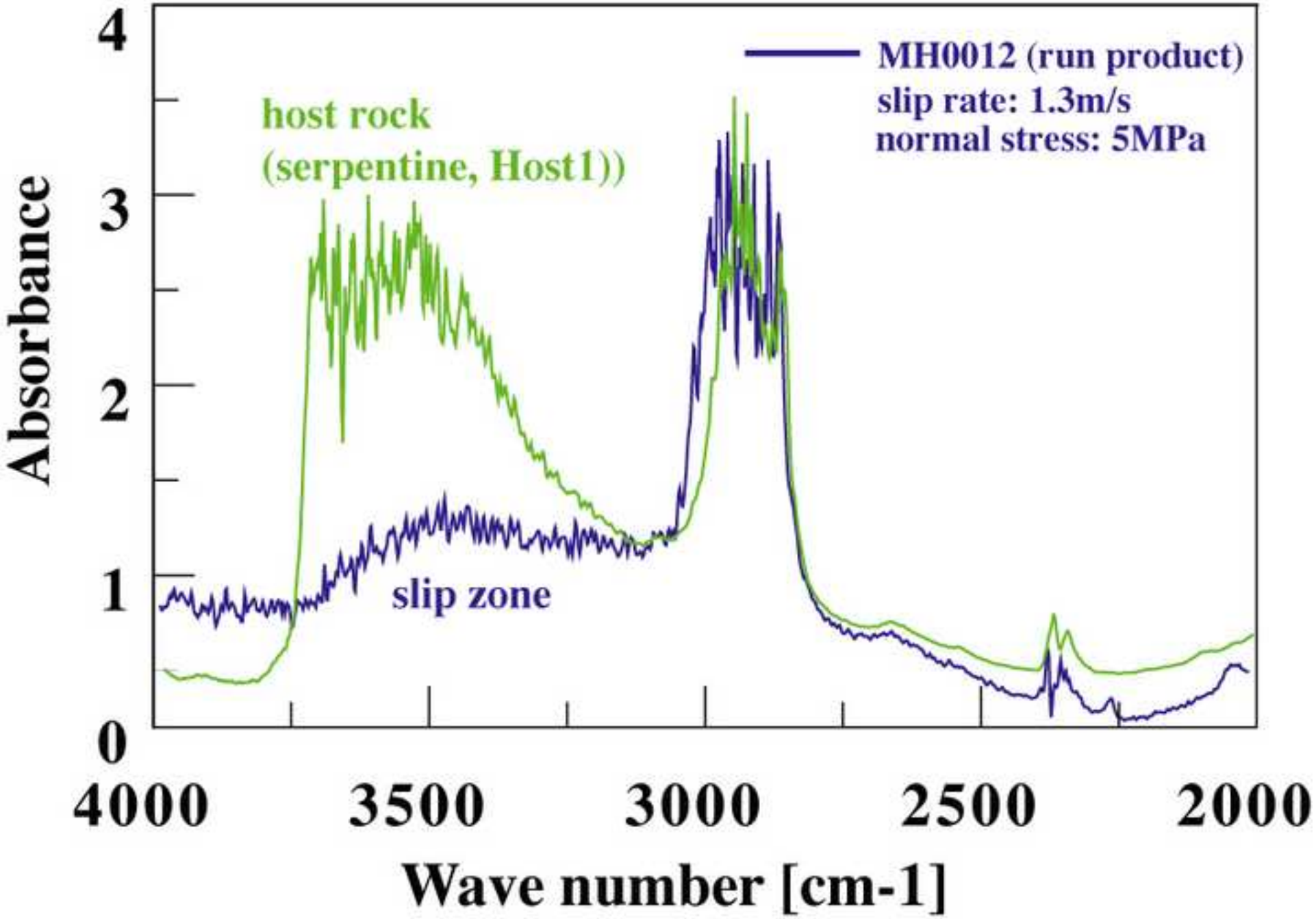

Figure12

Click here to download high resolution image

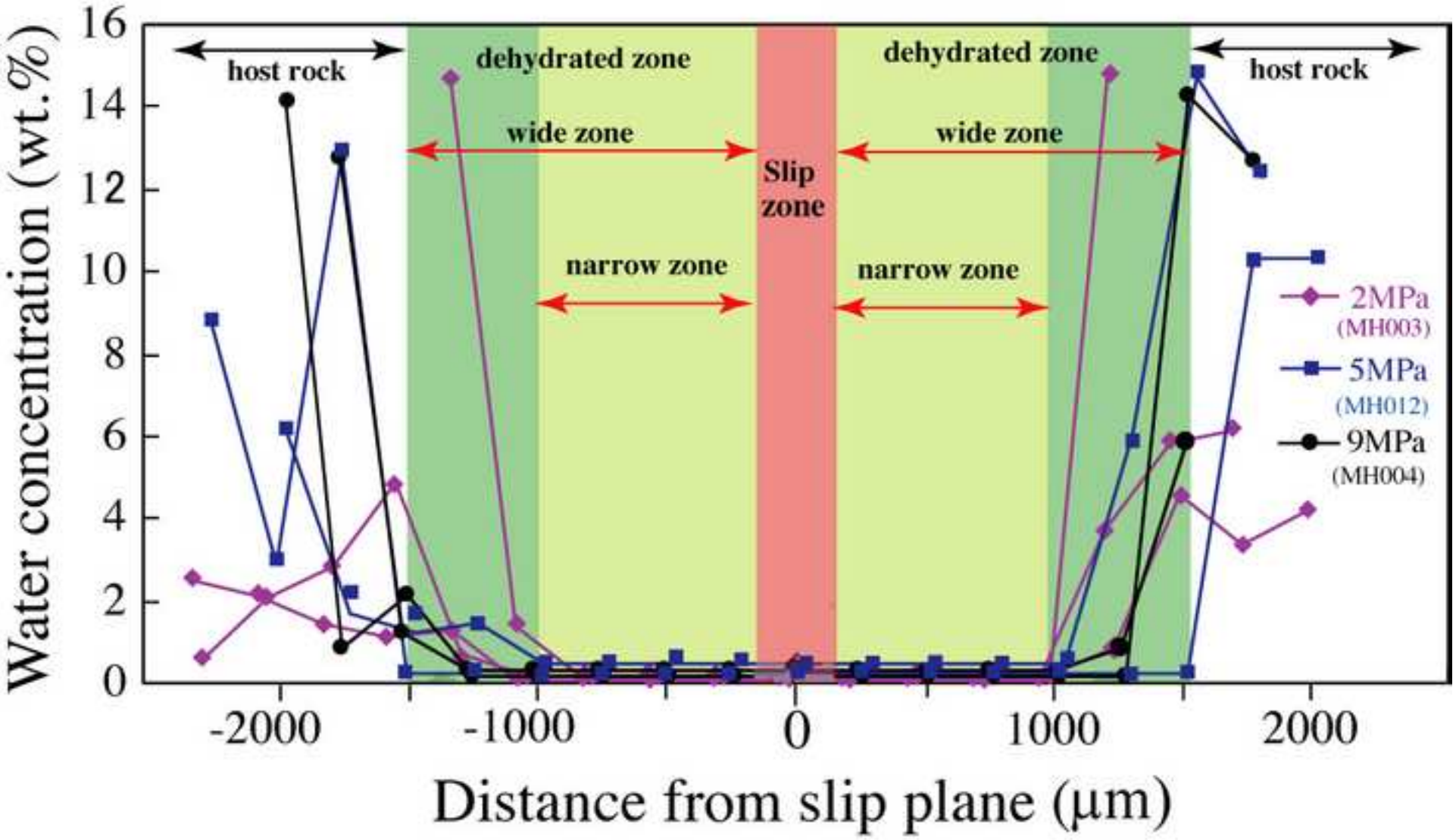

Figure13

Click here to download high resolution image

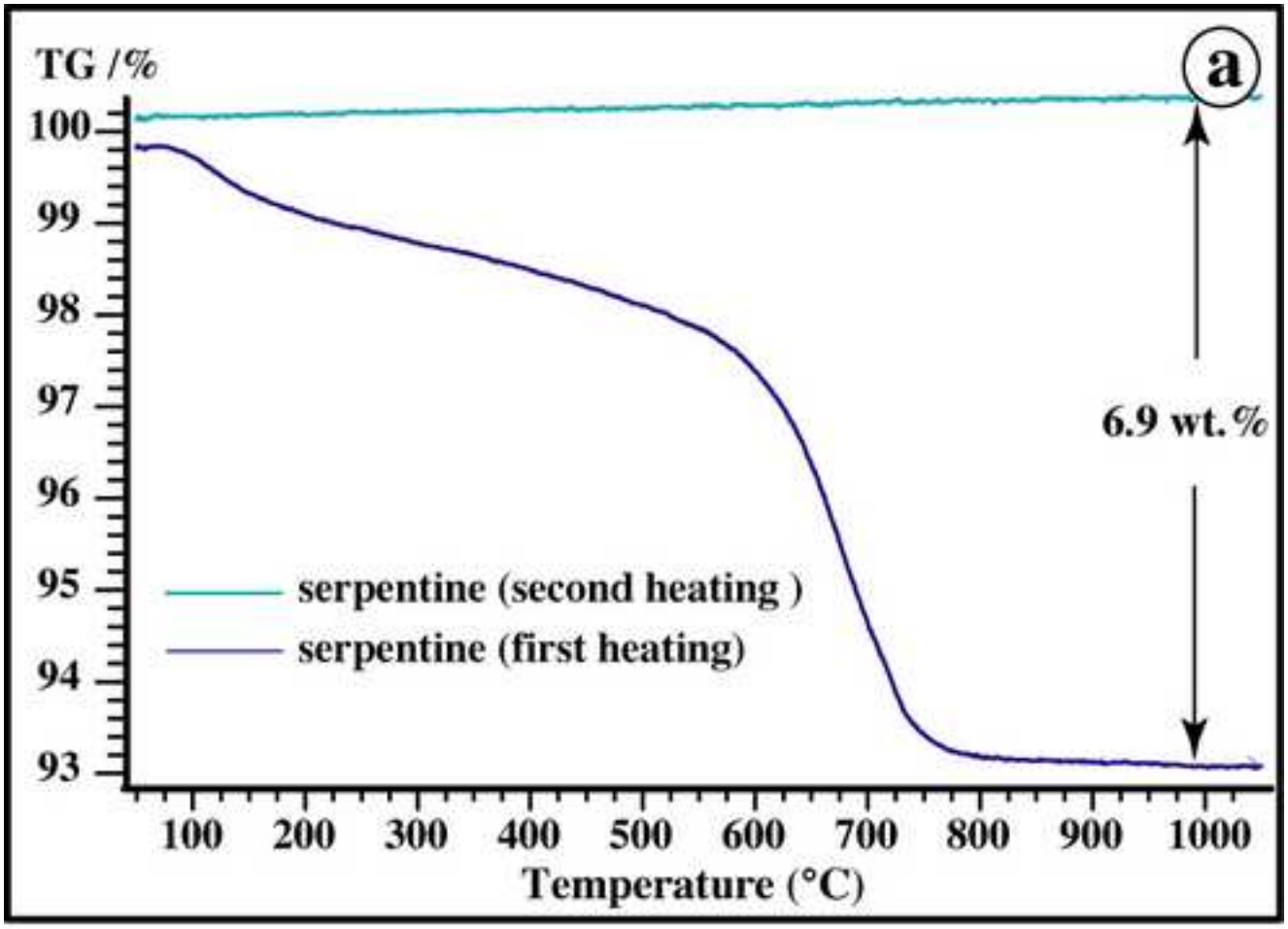

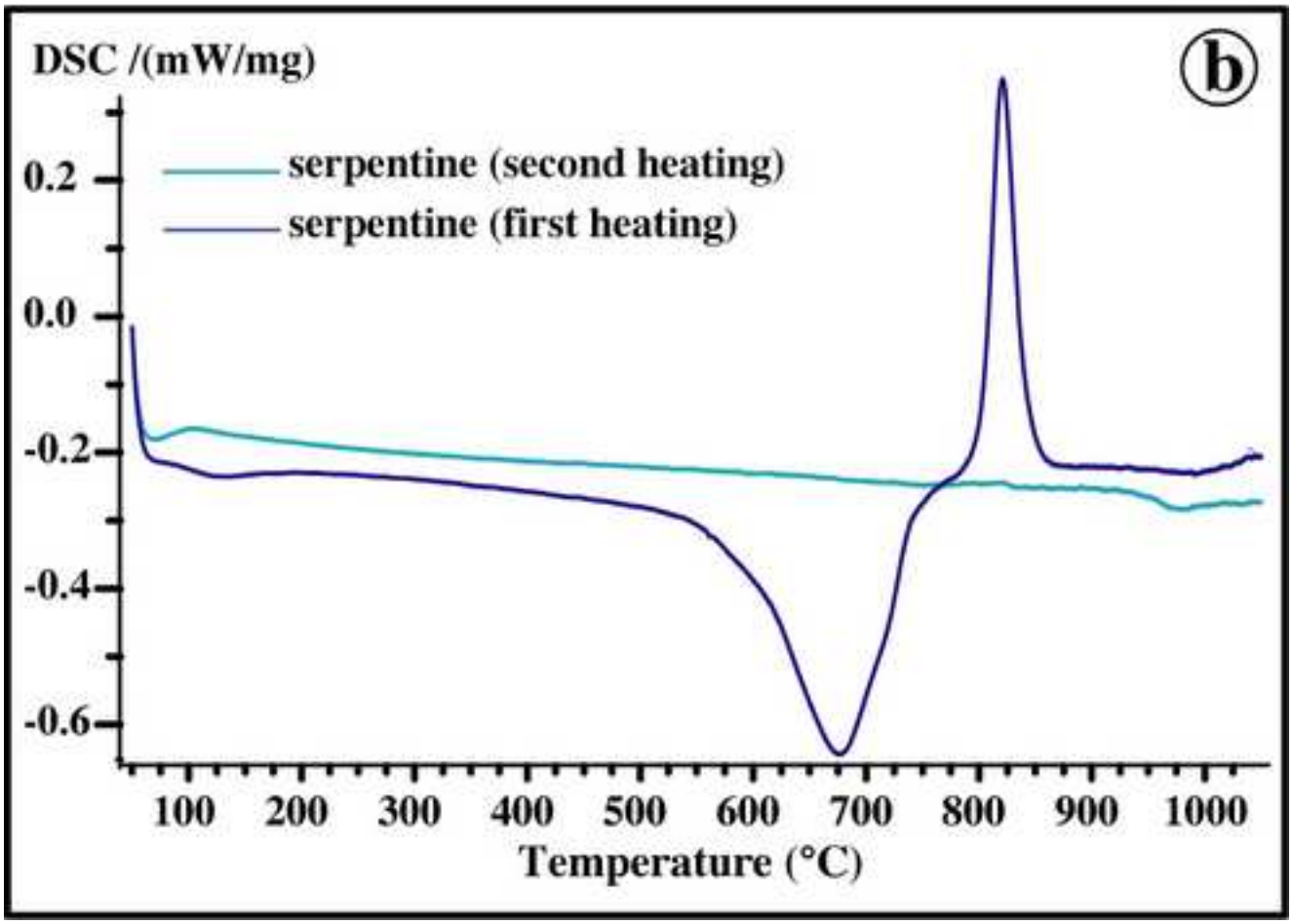

Figure14

Click here to download high resolution image

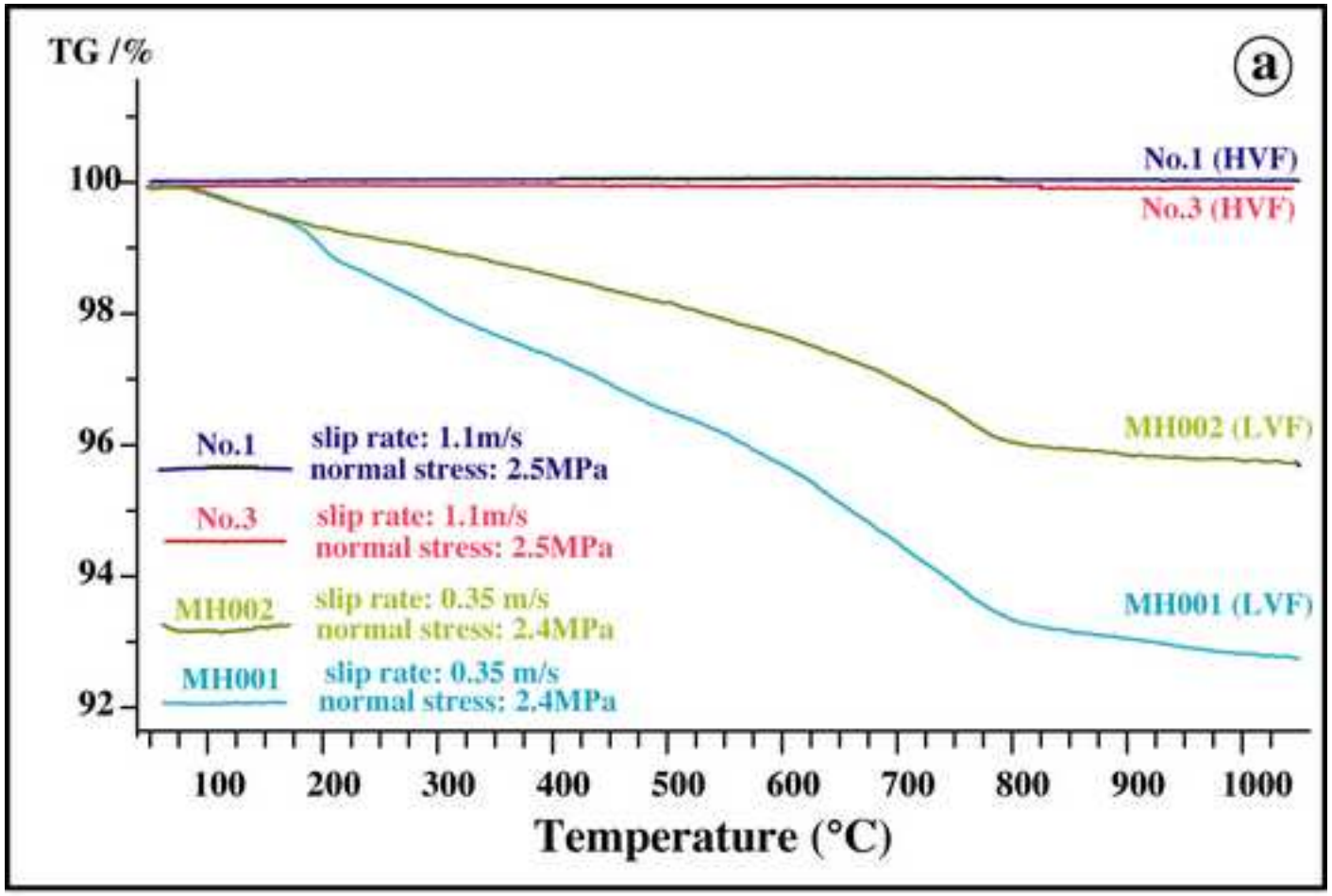

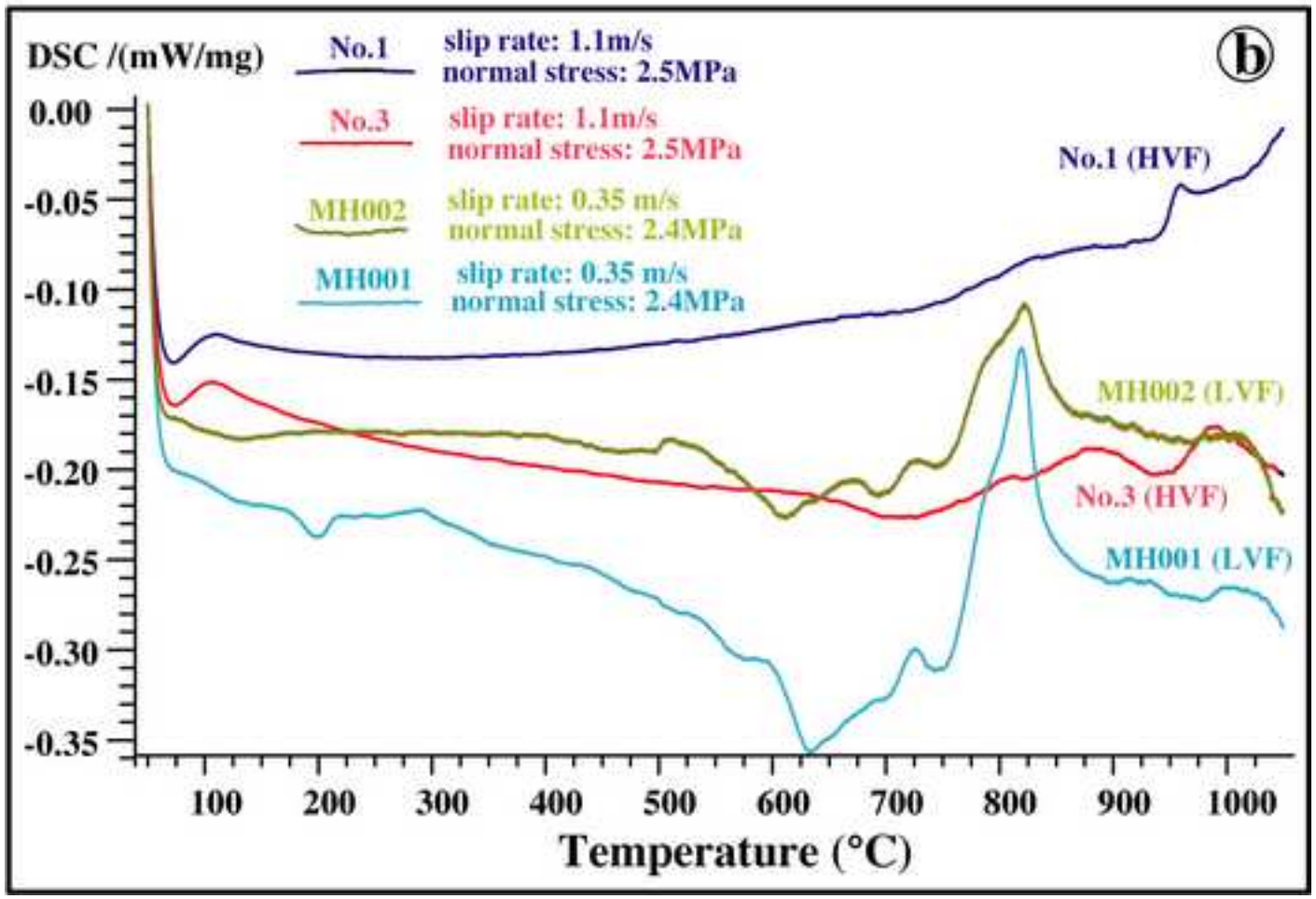

Table 1. Run products used for microscopic analyses.

Run number	Normal stress (MPa)	Slip rate (m/s)	Analytical method
No.1	2.5	1.10	TG-DSC analysis
No.3	2.5	1.10	TG-DSC analysis
MH001	2.4	0.35	TG-DSC analysis
MH002	2.4	0.35	TG-DSC analysis
MH003	2	1.10	FTIR analysis
MH004	9	1.10	FTIR analysis
MH012	5	1.31	FTIR analysis
HVF R001	6.5	1.10	Powder X-Ray analysis, EPMA
HVF R007	4	1.31	Powder X-Ray analysis, EPMA
THVR110	8.1	0.35	Frictional cofficient, shortening
HVF R012	5	1.31	Powder X-Ray analysis, EPMA

Table 2. Compositions of host rock (Host1, XRF) and serpentine (HS1-HS6, EPMA) and olivine (HO1-HO2, EPMA) materials in the host rock.

Sample No.	Host1	HS1	HS2	HS3	HS4	HS5	HS6	HO1	HO2
SiO2	41.580	41.322	40.648	41.944	40.068	41.422	42.828	40.576	41.185
TiO2	0.000	0.196	0.199	0.196	0.19	0.191	0.002	0.002	0.011
Al2O3	1.098	3.076	3.104	2.919	3.610	3.224	1.777	0.175	0.800
FeO	9.904	3.063	2.887	3.674	3.268	3.225	7.074	6.327	9.335
MnO	0.228	0.137	0.170	0.181	0.14	0.166	0.127	0.140	0.181
MgO	45.908	36.694	38.194	37.997	37.141	38.112	43.460	51.206	46.294
CaO	1.242	0.106	0.114	0.106	0.095	0.088	1.260	0.127	0.526
Na2O	0.034	0.086	0.108	0.093	0.125	0.111	0.074	0.010	0.036
K2O	0.012	0.060	0.063	0.059	0.073	0.065	---	0.011	0.010
V	0.029	0.213	0.185	0.211	0.208	0.211	---	0.026	0.002
Cr2O3	---	1.284	1.089	0.593	1.026	1.098	0.509	0.103	0.153
NiO	0.398	0.352	0.35	0.364	0.307	0.308	0.326	0.311	0.319
Total	99.973	86.588	87.11	88.337	86.249	88.219	97.438	99.013	98.852

XRF: X-ray fluorescence analysis; EPMA: Electron microprobe analysis;
FeO*: all Fe…; -not measured

Table 3. Chemical compositions of molten materials derived from the slip zone (M1-M8, EPMA).

Sample No.	M1	M2	M3	M4	M5	M6	M7	M8
SiO_2	42.366	44.776	39.494	44.441	44.073	43.809	41.185	43.629
TiO_2	0.015	0.012	0.001	0.025	0.022	0.003	0.011	0.000
Al_2O_3	1.971	2.814	0.000	3.010	2.371	2.003	0.800	2.044
FeO*	7.144	7.860	11.243	7.465	7.289	6.704	9.335	7.391
MnO	0.081	0.077	0.207	0.095	0.141	0.080	0.181	0.103
MgO	43.176	40.053	48.68	38.99	42.037	44.681	46.294	42.209
CaO	1.595	2.020	0.014	2.275	1.953	1.138	0.526	1.422
Na_2O	0.126	0.126	0.003	0.159	0.139	0.097	0.036	0.076
K_2O	0.006	0.005	0.002	0.011	0.000	0.000	0.010	0.014
V	0.035	0.034	0.029	0.024	0.003	0.022	0.002	0.015
Cr_2O_3	0.324	0.403	0.000	0.537	0.650	0.655	0.153	0.459
NiO	0.350	0.284	0.398	0.295	0.228	0.254	0.319	0.292
Total	97.188	98.464	99.558	97.328	98.908	99.446	98.852	97.654

EPMA: Electron microprobe analysis;
FeO*: all Fe

Table 4. Chemical compositions of serpentine minerals in the dehydration zones (Dh1-Dh9, EPMA).

Sample No.	Dh1	Dh2	Dh3	Dh4	Dh5	Dh6	Dh7	Dh8	Dh9
SiO2	47.462	45.76	46.881	45.543	44.184	46.035	44.832	44.243	46.742
TiO2	0.000	0.011	0.025	0.000	0.013	0.000	0.005	0.003	0.000
Al2O3	3.198	3.107	4.020	2.549	3.123	2.768	3.813	3.116	1.998
FeO*	4.023	4.245	4.482	4.225	4.059	3.978	4.016	3.826	3.794
MnO	0.031	0.054	0.031	0.035	0.012	0.031	0.030	0.050	0.027
MgO	43.347	42.058	42.198	45.431	45.116	44.074	43.134	44.208	43.458
CaO	0.249	1.424	0.056	0.027	0.018	0.015	0.048	0.398	1.797
Na2O	0.033	0.054	0.041	0.028	0.028	0.024	0.063	0.113	0.121
K2O	0.000	0.010	0.004	0.000	0.012	0.002	0.001	0.005	0.013
V	0.024	0.020	0.034	0.018	0.025	0.018	0.040	0.030	0.001
Cr2O3	0.419	0.236	0.870	0.463	0.889	0.476	1.441	1.605	0.621
NiO	0.151	0.160	0.134	0.181	0.214	0.165	0.223	0.157	0.163
Total	98.936	97.139	98.777	98.500	97.693	97.586	97.646	97.755	98.735

EPMA: Electron microprobe analysis;
FeO*: all Fe